Role of channels in the O_2 permeability of murine red blood cells
III. Mathematical modeling

Rossana Occhipinti[1]
Pan Zhao[1]
Fraser J. Moss[1]
Walter F Boron[1,2]

[1]*Department of Physiology & Biophysics*
Case Western Reserve University School of Medicine
Cleveland, OH 44106
and
[2]*Department of Medicine, and Department of Biochemistry*
Case Western Reserve University School of Medicine
Cleveland, OH 44106

Section: *Journal of Physiology*, Cell physiology

Running title: RBC O_2 permeability: Modeling

Keywords: hemoglobin, channel proteins

Correspondence and proofs:
Walter F Boron, MD, PhD
Department of Physiology and Biophysics
Case Western Reserve University
School of Medicine
10900 Euclid Avenue
Cleveland, OH 44106-4970
Phone: (216) 368 3400
Fax: (216) 368 5586
E-mail: Walter.Boron@case.edu

Key Points

- In this third of three papers, we develop a novel reaction-diffusion model for O_2 offloading from a red blood cell (RBC), treated as a sphere with diameter approximating RBC thickness.
- Using physical constants and parameter values from the literature and papers #1 and #2, we generate simulations that agree with hemoglobin desaturation (rate constant, k_{HbO2}) observed with RBCs from wild-type mice.
- To simulate k_{HbO2} decreases (9%, 17%, 30%) observed in RBCs from knockouts (KOs: aquaporin-1, Rhesus A-glycoprotein, both) we must decrease membrane O_2 permeability (P_{M,O_2}) by far greater percentages (22%, 36%, 55%).
- Analyses of simulated k_{HbO_2} sensitivity to kinetic and geometric parameters suggests that reasonable parameter-value changes cannot explain experimentally observed k_{HbO2} decreases in RBCs from KOs. Thus, experimentally observed k_{HbO2} decreases must reflect decreases in P_{M,O_2}.
- To accommodate for poikilocytes, we develop a linear-combination approach (poikilocytes + biconcave disks, BCDs) to extract the k_{HbO2} and P_{M,O_2} of just BCDs.

Abstract

In this third of three papers, we develop a reaction-diffusion model for O_2 offloading from a red blood cell (RBC), treated as a sphere with diameter approximating RBC thickness. Stopped-flow (SF) analysis (paper #1) of hemoglobin/oxyhemoglobin (Hb/HbO_2) absorbance spectra during O_2 efflux from intact murine RBCs show that membrane-impermeant inhibitor p-chloromercuribenzenesulfonate (pCMBS) reduces the HbO_2-deoxygenation rate constant (k_{HbO_2}) by ~64% . SF experiments shows that k_{HbO_2} falls by (i) 9% for aquaporin-1 knockouts (AQP1-KOs), (ii) 17% for Rhesus A-glycoprotein knockouts (RhAG-KOs), (iii) 30% for double knockouts (dKOs), and (iv) ~79% in dKOs+pCMBS. Here, we simulate HbO_2 dissociation (rate constant, $k_{HbO2\rightarrow Hb}$); HbO_2, Hb, and O_2diffusion through RBC cytosol; transmembrane O_2 diffusion; and O_2 diffusion through extracellular unconvected fluid (EUF) to bulk extracellular fluid. Informed by automated-hematology data (paper #1) and imaging–flow-cytometry data (paper #2), simulations predict that observed k_{HbO2} decreases cannot reflect changes in RBC size/shape or [Hb/HbO_2]. Instead, membrane O_2 permeability (P_{M,O_2}) must falls by (i) 22% to account for AQP1-KO data, (ii) 36% for RhAG-KOs, (iii) 55% for dKOs, and (iv) 91% for dKOs+pCMBS. Exploring predicted k_{HbO2} sensitivities to eight key parameters (e.g., [Hb/HbO_2], diffusion constants, $k_{HbO2\rightarrow Hb}$, thickness_{EUF}, diameter_{sphere}) shows that no reasonable change explain the k_{HbO_2} data. We introduce a linear-combination approach to accommodate for the presence of poikilocytes. Finally, contrary to common beliefs, the model predicts that the membrane represents >20% of total "resistance" to O_2 offloading, even for a WT mouse.

Introduction

Red blood cells (RBCs) are uniquely suited to perform the vital task of taking up oxygen (O_2) in the pulmonary capillaries, carrying this O_2 to the systemic capillaries, and there offloading the O_2 for consumption in the peripheral tissues. This journey of O_2 within the vertebrate body—and the oppositely directed journey of carbon dioxide (CO_2)—involves a series of convective and diffusive steps within and across the various components of the respiratory system.

Integral to the above sequence of events is an important series of membrane-permeation steps, both for O_2 delivery and CO_2 removal. Among the membranes that O_2 and CO_2 must traverse is the plasma membrane of RBCs. The mechanisms by which these gases move across cell membranes, including the RBC membranes, have been the subject of numerous investigations (Graham, 1829, 1833; Mitchell, 1830, 1833; Fick, 1855; Overton, 1895; Wroblewski, 1879; Hartridge & Roughton, 1927; Forster, 1964; Waisbren *et al.*, 1994; Nakhoul *et al.*, 1998; Cooper & Boron, 1998) and reviews (Stannett, 1978; Geers & Gros, 2000; Boron, 2010; Boron *et al.*, 2011; Endeward *et al.*, 2014; Cooper *et al.*, 2015; Michenkova *et al.*, 2021). Prior to the 1990s, two major schools of thought emerged. One, influenced by Krogh's cylinder model of O_2 diffusion from capillary to tissue, implicitly assumes that the RBC membrane offers no resistance to O_2 diffusion(Krogh, 1919; Kreuzer, 1982)—that is, the membrane behaves as a layer of water of equivalent thickness. The other school of thought, influenced by Overton's work on the lipoid nature of plasma membranes, is that the permeability of a membrane to a solute like O_2 depends only on the solubility of the solute in the lipid phase of the membrane (Overton, 1895, 1899).

The present paper is the third in a series of three interconnected papers that investigate the hypothesis that two membrane proteins that are abundant in the murine RBC membrane, aquaporin-1 (AQP1) and the Rh complex (RhCx)—comprising Rhesus blood group-associated A-glycoprotein (RhAG) and + Rhesus blood group D antigen (RhD)—represent a large fraction of the membrane permeability to O_2 (P_{M,O_2}) .

In the first paper (paper #1; Zhao *et al.*, 2025), we employ stopped-flow (SF) analysis of hemoglobin/oxyhemoglobin (Hb/HbO_2) absorbance spectra to measure the rate constant of Hb deoxygenation (k_{HbO_2}) in RBCs from mice genetically deficient in AQP1 (*Aqp1−/−*), RhAG (*Rhag−/−*), or both (*Aqp1−/−Rhag−/−*). In both wild-type (WT) mice and double knockouts (dKO), we also examine the effects of the inhibitors p-chloromercuribenzenesulfonate (pCMBS) and 4,4'-diisothiocyanatostilbene-2,2'-disulfonate (DIDS). Because k_{HbO2} depends on factors other than P_{M,O_2}, we also assess in paper #1 the rate constant of the dissociation $HbO_2 \rightarrow Hb + O_2$ in RBC hemolysates ($k_{HbO2\rightarrow Hb}$), and automated-hematological parameters, including mean corpuscular volume (MCV) and mean corpuscular hemoglobin concentration (MCHC).

We find that—compared to WT mice—k_{HbO_2} decreases by 9% in RBCs from AQP1-KOs, by 17% in RhAG-KOs, and by 30% in dKO. This work thus points towards roles for AQP1 and RhAG in enhancing O_2 permeation through RBC membranes.

In the second paper (i.e. paper #2; Moss *et al.*, 2025), we examine RBC morphology at a microscopic scale, and confirm that the RBCs from the KO and dKO mice are predominantly biconcave discs. We also use imaging flow cytometry (IFC) to assess RBC major diameter ($Ø_{Major}$). Together with MCV data from paper #1, $Ø_{Major}$ allows us to estimate RBC thickness—a critical piece of information for the simulations in this third (the present) paper in the series. The IFC data also shows that a small fraction of RBCs, more so in drug-treated cells, are poikilocytes, that is, non-biconcave disks (nBCDs). This is also critical information for this third paper because it sets the stage for a novel correction that we apply here. Finally, paper #2 includes a proteomic study that shows that the KO of one or both channels does not affect the apparent abundance of any of the 100 proteins with the greatest inferred abundance.

The purpose of this third (the present) paper in the series is to develop a reaction-diffusion model of O_2 offloading from RBCs, and to use this model—based only on first principles and informed by k_{HbO_2}, MCV, MCH, MCHC, $k_{HbO2\rightarrow Hb}$, and $Ø_{Major}$ data from the first two papers—to

simulate the SF data from the paper #1. We find that the simulations agree reasonably well with the time course of deoxygenation for RBCs from WT mice (measured as k_{HbO2} values) in paper #1. Note that our approach is not to adjust a variety of fitting parameters in an effort to reproduce the observed k_{HbO2}. Except for sensitivity analyses—when we examine how sensitive the simulations are to variations in specific fitting parameters—the only parameter that we vary is P_{M,O_2}, which we do to predict the P_{M,O_2} values that reproduce the experimentally determined time courses.

Taken together, the three papers argue strongly against each of two previously dominant—and quite opposite—schools of thought (addressed in the Discussion). One holds that RBC membranes offer no resistance whatsoever to O_2 diffusion. The other, posits that they do offer resistance, but that this resistance depends solely on the solubility of O_2 in RBC membrane lipids. Instead, our data are consistent with the notion that RBC membranes from WT mice offer ~150-fold more resistance to O_2 diffusion than an equivalently thick layer of water, and that channels—AQP1, RhCx, and an unidentified channel(s)—account for 90% of P_{M,O_2}.

Methods

Mathematical modeling and simulations

Model formulation. To examine the possibility that changes in RBC parameters—decreases in $k_{HbO2 \rightarrow Hb}$, increases in MCHC (i.e., $[Hb+HbO_2]_i$), decreases in diffusion constants (i.e., intra-/extracellular D for O_2; extracellular D for HbO_2, Hb), increases in the unconvected-fluid layer that surrounds the cell, or increases in intracellular diffusion distances (i.e., sphere diameter), or—can explain our observed decreases in k_{HbO_2}, we developed a distributed (i.e., space-dependent) and dynamic (i.e., time-dependent) reaction-diffusion mathematical model of an RBC—simplified as a perfectly symmetric sphere with diameter equal to the thickness of the RBC. Note that the thickness of the biconcave disk near its edge (~2 μm)—not the major diameter (~6.8 μm for mice)—is the dimension of the RBC (when it is a BCD) that is critically important for gas exchange, as pointed out by several authors (Roughton, 1932; Ponder, 1948; Forster, 1964; Endeward, 2012). Previous modelers have used a sphere in their simulations of an RBC (Vandegriff & Olson, 1984*a*; Williams & Kutchai, 1986; Deonikar & Kavdia, 2013; Deonikar *et al.*, 2014), matching the diameter of the sphere to $Ø_{Major}$. As described below, our geometrical approach differs in that we chose the diameter of the sphere to match the minor diameter of a torus that has the same volume as the RBC. In our model (see Figure 1*A*), the spherical RBC is enveloped by a layer of extracellular unconvected fluid (EUF), which is in turn enveloped by the bulk extracellular fluid (bECF). The model accounts for diffusion of O_2, Hb, and HbO_2 within the intracellular fluid (ICF). Only O_2 can move—via diffusion—between the ICF and EUF (i.e., across the plasma membrane, PM), within the EUF (which lacks Hb and HbO_2), and between the EUF and bECF. Reactions among O_2, Hb, and HbO_2 occur only in the ICF.

Assuming spherical-radial symmetry, then for each solute S (i.e., O_2, Hb, and HbO_2), the concentration (C_S) changes in time (t) and space according to the reaction-diffusion equation

$$\frac{\partial}{\partial t} C_S(t,r) = \underbrace{\frac{1}{r^2}\frac{\partial}{\partial r}\left(D_S(r)\, r^2 \frac{\partial}{\partial r} C_S(t,r) \right)}_{\text{Diffusion term}} + \text{Reaction term}, \quad (1)$$

where r is the radial distance from the center of the RBC, and D_S is the diffusion coefficient of solute S. Figure 1*B* shows the computational domain.

Kinetics of the oxygen-hemoglobin reaction. We model the binding of O_2 to Hb (and dissociation of O_2 from HbO_2)—that is, the reaction term in Equation (1)—as a simple, one-step reaction in which we use a version of the variable-rate-coefficient (VRC) approach proposed by Moll (Moll, 1968). Thus, we assume that each hemoglobin tetramer (Hb_4) is replaced by four independent heme molecules, 4×Hb, and that each heme combines with O_2 via the one-step reaction

$$\mathrm{HbO_2} \underset{k'}{\overset{k}{\rightleftharpoons}} \mathrm{Hb} + \mathrm{O_2}, \quad (2)$$

where k and k' are, respectively, the dissociation and association reaction rate constants.[1] Rather than assuming that both k and k' are constant—an assumption that would lead to a non-realistic hyperbolic hemoglobin-oxygen saturation curve—we follow a version of Moll's VRC approach, in which we assume that only one of the two reaction rates is constant, while the other one becomes a function of the partial pressure of O_2 (P_{O_2}) so that the mathematical representation of the hemoglobin-oxygen saturation curve corresponds to the measured sigmoidal curve. Yap and Hellums (1987) showed that the VRC model is appropriate in the physiological range, and avoids

[1] Note that k in the above equation is analogous to $k_{HbO_2 \to Hb}$ (the rate constant for deoxygenation of HbO_2 in an RBC hemolysate). k' is analogous to $k_{Hb \to HbO_2}$ (the rate constant for the reversed reaction). For simplicity, in this section "Kinetics of the oxygen-hemoglobin reaction" we use k and k' to indicate $k_{HbO_2 \to Hb}$ and $k_{Hb \to HbO_2}$, respectively.

the use of the more complex Adair model . In his VRC approach, Moll assumed that k' is constant and k is a function of P_{O_2}. However, Clark *et al.* (1985) pointed out that the function used by Moll to describe k as a function of P_{O_2} approaches infinity as P_{O_2} approaches zero . These last authors overcame this problem by assuming that k is constant and k' is a function of P_{O_2}, as described by

$$k' = k \frac{1}{\alpha \times P_{O_2}} \left(\frac{P_{O_2}}{P_{50}} \right)^n , \qquad (3)$$

where α is the solubility coefficient for O_2 in water, P_{50} is P_{O_2} when [Hb] = [HbO_2], and n is the Hill coefficient. With this choice and $n > 1$, k' approaches zero as P_{O_2} approaches zero. Thus, in our model, we follow Clark's variation of the VRC approach, which we implement with the slight modification of substituting [O_2] for P_{O_2}:

$$k' = k \frac{[O_2]^{n-1}}{\left([O_2]_{50}\right)^n} . \qquad (4)$$

Calculation of RBC thickness based on the geometry of a torus. For each mouse strain, we calculate the RBC thickness as follows. We start from the mean major diameter of all RBC-related cell types[2] (e.g., $Ø_{Major}$ = 6.80 μm for WT cells; see paper #2)—a measured value—and assume that the RBC is a torus, the outer diameter (OD_{Torus}) of which equals the aforementioned $Ø_{Major}$ (i.e., 6.80 μm in our example). Next, we use the mean corpuscular volume (e.g., MCV = 47.9 pl for WT cells; see paper #2)—also a measured value, which we assume to be equal to the volume of the torus (V_{Torus})—to calculate the minor radius (r) of the torus (equivalent to half the thickness of the RBC). Thus, r is a root of the polynomial:

[2] These include immature RBCs (i.e., nucleated cells, reticulocytes, and spherocytes) as determined by imaging flow cytometry in paper #2.

$$2\pi^2 r^3 - \pi^2 \left(OD_{\text{Torus}}\right) r^2 + V_{\text{Torus}} = 0. \qquad (5)$$

The calculated value for the WT cells is r = 1.01 μm. In Table 2, we provide—for each of the 4 mouse strains—the computed values for r, the major radius of the torus (R), and the diameter ($Ø_{\text{Sphere}}$) of the equivalent sphere = $2r$ (i.e., RBC thickness). The equivalent sphere diameters serve as inputs to our mathematical model.

Calculation of Hb content. For each mouse strain, we calculate the concentration (in mM) of total Hb tetramers as follows. Based on the hematology data[3] reported in paper #2—specifically, the MCH (in pg) and MCV (in fl)—and using a value of 64316 g/mol for the molecular weight of mouse Hb, we calculate the MCHC (in mM). For WT mice, the concentration of total Hb tetramers was ~4.7 mM. However, because our mathematical model deals with monomers, we calculate the concentration of total of Hb monomers using 4 × MCHC. In the case of RBCs from WT mice, this figure is 18.73. Table 2 lists this value, as well as the comparable values for the other three genotypes. These values inform our mathematical model.

Computational model. In order to solve the system of the three reaction-diffusion equations (1)—one for O_2, one for Hb monomers, and one for HbO_2 monomers—we set the following boundary conditions.

At the center of the RBC, we posit the no-flux Neumann boundary condition:

$$\frac{\partial C_{\text{S}}}{\partial r}(t,0) = 0.$$

[3] These hematology data pertain to the subset of mice used in the imaging flow cytometry and MMM studies.

At the interface between the ICF and the EUF (i.e., at the PM), we establish continuity of Fick's diffusive flux:

$$D_S(R+)\frac{\partial}{\partial r}C_S(t,R+) = P_{M,S}\cdot(C_S(t,R+) - C_S(t,R-)).$$

$$D_S(R-)\frac{\partial}{\partial r}C_S(t,R-) = P_{M,S}\cdot(C_S(t,R+) - C_S(t,R-)).$$

Here, R is the radius of the sphere, $C_S(t, R-)$ is the time-dependent concentration of solute S in the aqueous phase adjacent to the intracellular (−) side of the PM; $C_S(t, R+)$, the comparable value on the extracellular (+) side; and $P_{M,S}$ is the true permeability[4] of the membrane to solute S. Because O_2 is the only solute that can diffuse across the PM, $P_{M,S} \neq 0$ only for $S = O_2$.

In the bECF, we assign Dirichlet boundary conditions and assume that the concentration of O_2 is constant and equal to zero. This assumption is the mathematical equivalent of the annihilation of O_2 by sodium dithionite in our SF reaction cell (see paper #1).

Finally, we set the initial conditions by assuming that, at the beginning of the experiment (i.e., our simulation), no O_2 is present in the EUF, and the free [O_2] everywhere inside the RBC is that dictated by Henry's law for a gas mixture containing 21% O_2. The initial concentrations of O_2, Hb, and HbO_2 in the ICF are those reported in Table 1 for RBCs from WT mice, and in Table 2 for RBCs from mice of each of four genotypes.

---

[4] This is the "permeability" computed on the basis of concentrations immediately adjacent to the two sides of the membrane. Physiologists usually define permeability operationally, based on the respective concentrations in the bulk intra- and extracellular fluids (see Boron, 2010).

We solve the system of the three reaction-diffusion equations (i.e., Eqn (1) for the solutes O_2, Hb, and HbO_2) using the method of lines and the approach described by Somersalo et al for the numerical implementation of the diffusion component (Somersalo *et al.*, 2012). We solve the resulting system of time-dependent ordinary differential equations in Matlab R2015a using the stiff solver ode15s with AbsTol=RelTol=1e–12. The Matlab code is based on the original implementation of Somersalo et al.

Parameter values. Table 1 lists the parameter values used in the simulation for RBCs from WT mice. Table 2 lists the parameters that we measured in the present study, specific for each of the 4 genotypes; we use these values for computing values for Figure 3. All parameter values correspond to a temperature of 10°C, the temperature at which we perform the stopped-flow experiments (see paper #1). For parameter values not available at the temperature of 10°C, we derive them using Arrhenius equation and values at 25°C and 37°C from references indicated in Table 1. We use this approach for calculating the diffusion coefficient of HbO_2 and HbO_2 in the bulk ICF.

For the diffusion coefficient of O_2 in the bulk ICF, the commonly used value (adjusted for 10°C using the Arrhenius equation, as described above) is 5.09×10^{-6} cm^2 s^{-1} (Clark *et al.*, 1985). Recently, Richardson et al (Richardson *et al.*, 2020) obtained the much lower value of 4.5907×10^{-7} cm^2 s^{-1} (see Discussion). However, this latter value is likely to be an underestimate because Richardson et al used a very low extracellular concentration of NDT (i.e., 1 mM vs. the 25 mM in the present study). This low $[NDT]_o$ would have increased the thickness of the EUF (ℓ_{EUF}) surrounding the RBC, and thus increased the resistance to the diffusion of O_2 away from the RBC surface (Coin & Olson, 1979; Vandegriff & Olson, 1984*b*; Holland *et al.*, 1985). Thus, to some extent, the authors attributed to the ICF a component of total resistance to O_2 diffusion that was actually due to the EUF. The result is an inappropriately low estimate for the intracellular diffusion constant for O_2. Because we do not know the magnitude of this error, we chose to compute the

arithmetic mean of the commonly used value of 5.09×10^{-6} cm^2 s^{-1} and the more recent value of 4.5907×10^{-7} cm^2 s^{-1}. The result is 2.7745×10^{-6} cm^2 s^{-1}, which we report in Table 1.

Because the molecular weight of O_2 is much less than the molecular weight of Hb, and because the diffusion coefficient mainly depends on molecular weight, we assume that the diffusion coefficients of monomeric HbO_2 and Hb are the same (Popel, 1989). We assume that the permeability of the RBC plasma membrane to O_2 is 0.15 cm/sec, the value estimated by Endeward et al (Endeward *et al.*, 2006) for the permeability of the RBC plasma membrane to CO_2.

Simulation of time course of HbO_2 deoxygenation, and estimation of k_{HbO_2}. Using the reaction-diffusion model, we simulate the time course of the decline of HbO_2 saturation (i.e., HbSat = $[HbO_2]/([Hb]+[HbO_2])$ vs. time, employing hematological and morphological data that we gathered for RBCs from WT mice (see Table 1). Because neither the actual nor the simulated time courses of HbO_2 desaturation are precisely exponential, we compute k_{HbO_2} from simulations in a manner analogous to that for our physiological data (see paper #1): we determine the time for the simulated HbSat to fall to $1/e \cong 37\%$ of its initial value (i.e., $\tau_{Quasi} \cong t_{37}$), and then compute k_{HbO_2} as $1/t_{37}$.

Data availability

The data supporting the findings of this study are available within the paper and its Supplementary Information files. Any further relevant data are available from the corresponding author upon reasonable request.

Results

The overarching hypothesis of papers #1 and #2 is that AQP1, RhAG, and at least one other RBC membrane protein contribute in a major way to the O_2 permeability of murine RBC membranes.

From a technical perspective, the purpose of this third paper is to develop a reaction-diffusion model—our shorthand for this macroscopic mathematical model is MMM—that is applicable to RBCs in the stopped-flow studies of paper #1. Because our MMM incorporates Fick's first law of diffusion to describe transmembrane O_2 efflux (see Methods) we can relate the input parameter P_{M,O_2}—incorporated into the D_S term in Eqn (1)—to the output parameter MMM-k_{HbO_2}. As noted in the Introduction, in our simulations, we do not adjust myriad parameter values to match physiological data, but rather use the model to predict—from first principles—the time course of HbO_2 desaturation, which yields MMM-k_{HbO_2}. The input parameters for the simulations are physical constants and values obtained from the literature (see Table 1) as well as values obtained in automated-hematology studies and imaging flow cytometry in papers #1 & #2 (see Table 2). The latter—which include MCV, MCH, and $Ø_{Major}$—allow us to determine values for RBC thickness and total Hb concentration and thereby perform simulations that mimic as closely as possible the conditions of our physiological experiments.

From a philosophical perspective, our purpose the present paper is to use simulations based on the MMM to make a series of estimates of P_{M,O_2} that generate values of k_{HbO_2} (MMM-k_{HbO_2}) that allow us to hone in on our best estimate of P_{M,O_2} in a particular set of stopped-flow experiments in paper #1.

If our hypothesis is correct, RBCs from mice genetically deficient in AQP1, RhAG, or both should have lower P_{M,O_2} values when compared to RBCs from WT mice. In order to test our hypothesis, we must assess P_{M,O_2} from experimental data. In paper #1, we use SF absorbance

spectroscopy to measure k_{HbO_2} of RBCs from mice genetically deficient in AQP1, RhAG, or both. We find that, when compared to WTs, k_{HbO_2} decreases by 9% in AQP1-KOs, 17% in RhAG-KOs, and 30% in dKOs. Moreover, k_{HbO_2} decreases by 53% in dKO RBCs treated with DIDS, and by 78% in dKO RBCs treated with PCMBS. One might immediately ask why the sum 9% + 17% is not precisely 26%? The answer, aside from experimental and rounding errors, is that P_{M,O_2}—the presumed target of our genetic and pharmacological manipulations—is only one element that contributes to MMM-k_{HbO_2} (see Figure 1*A*), resulting (as we shall see later) in a curvilinear dependence of P_{M,O_2} on log(k_{HbO_2}).

In the following sections we show that, by informing the model with reasonable parameter values and internally consistent (i.e., gathered in our laboratory) hematology and flow cytometry data, our MMM model provides reasonable estimates of the time course of HbO_2 desaturation and corresponding MMM-k_{HbO_2}. Moreover, the model confirms that decreases in the value of k_{HbO2} correspond to decreases in P_{M,O_2}, thereby supporting the hypothesis that membrane proteins like AQP1 and the mouse Rh complex (Rh_{Cx} = RhAG + RhD) contribute to P_{M,O_2}.

Simulations of O_2 efflux from the RBC of a control WT mouse

Our first goal was to establish an in-silico experiment that would mimic O_2 efflux from a control (i.e., not pretreated with inhibitors) RBC of a WT mouse. For this simulation, our input parameters are those reported in Table 1, which includes physical constants and values obtained from the literature as well as values for RBC thickness and total Hb concentration obtained from our hematological and morphological data (i.e., MCV, MCH, $Ø_{Major}$) of WT mice (see Table 2, first column).

Figure 2 shows results of this simulation. Panels *A*, *B*, and *C* show the time courses of the intracellular concentrations of free O_2, HbO_2, and Hb—integrated over the entire volume of the cytoplasm—as O_2 diffuses out of the cell. As expected, because O_2 is leaving the cell, the

intracellular concentration of free O_2 decreases (Figure 2*A*). At the same time, intracellular [HbO_2] decreases (Figure 2*B*) and [Hb] increases (Figure 2*C*), reflecting the action of the net reaction $HbO_2 \rightarrow Hb + O_2$, which consumes HbO_2 to produce Hb and O_2 and continues until HbO_2 is fully depleted.

Figure 2*D* shows the time course of the decline of HbO_2 saturation, from which we calculate the MMM-k_{HbO_2} of untreated WT RBCs (see Methods). The model predicts a MMM-k_{HbO_2} of ~3.99 s^{-1}. Because in our simulation we assume that all RBCs are biconcave disks (i.e., no deformed RBCs are presented and we compute RBC thickness using the torus approach), our MMM-k_{HbO_2} here in paper #3 corresponds to shape-corrected (SC) k_{HbO_2} values in paper #1. Comparing the MMM-k_{HbO_2} value of ~3.99 s^{-1} with the SC-k_{HbO_2} values for untreated WT RBCs, we observe that our MMM-k_{HbO_2} is ~23% higher than the lowest HC-k_{HbO_2} value (3.24 s^{-1}) in paper #1 but ~2.5% lower than the highest SC-k_{HbO_2} value (4.09 s^{-1}) in paper #1. Thus, our MMM, based on first principles, provides a reasonable estimate for the k_{HbO_2} of untreated WT RBCs. Hereafter, we will consider this simulation as the one describing an in-silico O_2-efflux experiment with a control WT RBC and we will refer to it as the control "MMM-WT RBC".

Predicted k_{HbO_2} values from simulations of control RBCs from WT and KO mice, as informed by genotype-specific hematological, morphological, and kinetic data

Besides P_{M,O_2}, the MMM-k_{HbO_2} that describes O_2-offloading from RBCs depends on several genotype-specific parameters: $Ø_{Sphere}$ (which in turn depends on MCV, $Ø_{Major}$, and RBC shape), [Total Hb]$_i$ (computed from MCHC), and $k_{HbO_2 \rightarrow Hb}$ (determined on SF experiments on RBC hemolysates). To investigate whether the decreases in k_{HbO_2} observed in RBCs from KOs (see paper #1) could be explained by changes in parameters other than P_{M,O_2}, we as a first step gathered the requisite genotype-specific data in paper #1 and paper #2. We provide these parameter values in Table 2. Note the trend (from left to right) for MCV in increase in the KOs, but for

MCHC to decrease. In addition, using a battery of methodologies to assess RBCs shape (blood smears, still/video images of living RBCs, and imaging flow cytometry), we find that ~98% of control RBCs, both from WTs and dKOs, are biconcave disks (see paper #2).

To assess the effects of the genotype-specific differences summarized in Table 2, we perform simulations in which we mimic control RBCs (i.e., not pretreated with inhibitors) from WT, AQP1-KO, RhAG-KO and dKO mice. Note that the simulation for a control WT RBC is the same one that yielded the MMM-k_{HbO_2} of 3.99 s^{-1} in the previous section. We simulate O_2 efflux from RBCs of AQP1-KO, RhAG-KO, and dKO mice using the same parameter values (including P_{M,O_2}) that we used for the control WT RBC (see Table 1) with the exception of the genotype-specific values (see Table 2) for $Ø_{Sphere}$ (mimicking RBC thickness) and [Total Hb monomers]$_i$ (a surrogate for MCHC).

Figure 3 shows these simulations for each of the four genotypes. Because in these simulations we ignore the presence of nBCDs (i.e., we assume that all RBCs are BCDs), our MMM-k_{HbO_2} values are analogous to the SC-kHbO_2 values for SF experiments in paper #1.

The solid green bar in Figure 3 corresponds to MMM-$k_{HbO_2} \cong 3.99$ s^{-1} for an untreated WT RBC, analogous to the green bar in paper #1 with SC-$k_{HbO_2} \cong 4.09$ s^{-1}.

The pink bar in Figure 3 simulates a control AQP1-KO RBC; MMM-$k_{HbO_2} \cong 4.03$ s^{-1}, which is a predicted 1.1% increase vs. 3.99 s^{-1}, rather than the 9% decrease observed in paper #1.

The blue bar in Figure 3 simulates a control RhAG-KO RBC; its MMM-k_{HbO_2} of 3.81 s^{-1} represents a predicted decrease of 4.4%, rather than the 17% decrease observed in paper #1.

Finally, the purple bar in Figure 3 simulates a control dKO RBC; its MMM-k_{HbO_2} of 3.84 s^{-1}, is a decrease of only 3.7% vs. WT, rather than the ~30% decrease in paper #1.

Thus, we conclude that the genotype-specific changes reported in paper #1 and paper #2—and summarized here in Table 2 —cannot explain the observed KO-induced decreases in SC-k_{HbO2} in paper #1. We intuit that the effects of anti-parallel increases in MCV and decreases in MCHC tend to cancel, and thereby tend to minimize impact on MMM-k_{HbO2} values. We examine this possibility in the sensitivity analyses, below. We conclude that KO-induced variations in RBC dimensions, $[Hb_{tot}]_i$, and $k_{HbO2 \rightarrow Hb}$ cannot account for the KO-induced decreases in SC-k_{HbO2} observed in paper #1.

Predicted dependence of O_2 offloading (k_{HbO2}) on the O_2 permeability of RBC membrane (P_{M,O_2})

In the previous sections, we show that our MMM—with a fixed P_{M,O_2} and genotype-specific values for other parameters—can mimic the time course of O_2 offloading (i.e., MMM-$k_{HbO2} \cong$ SC-k_{HbO2}) for a control RBC from a WT mouse, but not for control RBCs from any of our three KO groups. Clearly, we must invoke some other parameter to account for the control and KO data in paper #1 and, by extension, the paper-#1 data on inhibitors and KO+inhibitors. We hypothesize that this other parameter is P_{M,O_2}. (In the case of drug-treated RBCs, we will apply a shape correction, described below, to accommodate the appearance of poikilocytes).

Having established an in-silico approach for control/WT experiments, we can now employ the model to answer the two key questions that are at the core of our investigation:

1. What is the dependence of MMM-k_{HbO2} on P_{M,O_2}? This will help us understand the extent to which observed decreases in SC-k_{HbO2} in paper #1 correspond to decreases in P_{M,O_2}?
2. Can we use physiological k_{HbO2} measurements to make predictions about P_{M,O_2}?

To answer these questions, we employ the model that mimics a control WT RBC (i.e., input parameter values listed in Table 1) and perform a series of more than 70 simulations in which we

systematically vary P_{M,O_2} while holding all other parameters constant. Throughout, we assume that the RBCs are biconcave disks so that we need not accommodate for shape changes. Thus, by definition, the MMM-k_{HbO_2} is analogous to the SC-k_{HbO_2}. The continuous curve in Figure 4 is a semi-logarithmic plot showing the dependence of MMM-k_{HbO_2} (y-axis) on P_{M,O_2} (x-axis, scaled logarithmically). The shape of this curve depends on the parameters in Table 1.

The point at the extreme upper-right represents the hypothetical situation in which we assume that the plasma membrane—as is implicit in Krogh's calculations—is a thin film of H_2O of equivalent thickness. That is, for the plasma membrane, we assume that the diffusion constant D_{O_2} has the same value as in free water, namely 1.3313×10^{-5} cm^2/sec cm s^{-1}, which translates to a P_{M,O_2} of ~22.63 cm s^{-1}. In our simulations, this value generates a MMM-k_{HbO2} of 5.9953 s^{-1}. For the given geometric, hematologic, and kinetic parameters, this point represents the maximum-possible values for P_{M,O_2} and thus the maximum rate of O_2 offloading.

The point labeled "H_2O membrane" corresponds to a simulation in which we assumed that P_{M,O_2} is equal to that of an equivalent thin film of H_2O. This point has the coordinates (P_{M,O_2} = 22.63 cm s^{-1}, k_{HbO2} = 5.9953 s^{-1}).

What is the position of a WT RBC on this curve? Recall that (1) WT RBCs have an nBCD prevalence of 1.41% (see paper #2) and (2) nBCDs have a lower O_2-offloading rate that BCDs. In somewhat of an arbitrary exercise, let us assume that the MMM-k_{HbO_2} of 3.99 s^{-1} that we have already generated in a simulation using P_{M,O_2} = 0.15 cm s^{-1} does not pertain to a pure population of BCDs, but rather to a mixture of 98.59% BCDs and 1.41% nBCDs. In other words, we imagine that the MMM-k_{HbO_2} of 3.99 s^{-1} is our best simulation of the hemolysis-corrected k_{HbO_2} from physiological experiments, and the P_{M,O_2} of 0.15 cm s^{-1} is a provisional estimate of the actual P_{M,O_2} that we assume to be the same for both BCDs and nBCDs in the RBC mixture. What is the actual P_{M,O_2}? As we will see below when we introduce the shape correction, the actual P_{M,O_2} of a BCD/nBCD must be somewhat higher—about 3.1% in this case—than our previously assumed

"provisional" value of 0.15 cm s^{-1} to account for the measured 1.41% prevalence of nBCDs, and the measured nBCD diameter (which is larger than the thickness of a BCD). As a result, the computed SC-k_{HbO2} (which represents just BCDs) must be somewhat higher—about 1.0% in this case—than the provisional value of 3.99 s^{-1} (which represents the BCD+nBCD mixture). Thus, the point labeled "WT" in Figure 4 has the shape-corrected coordinates (P_{M,O_2} = 0.1546 cm s^{-1}, k_{HbO2} = 4.0358 s^{-1}) and represents a pure population of BCDs. Viewed differently, the provisional WT point (not shown)—representing a mixture of 98.59% BCDs and 1.41% nBCDs—would still lie on the sigmoidal curve, but almost imperceptibly to the lower-left of the labeled WT point.

Note that the WT point in Figure 4 has a P_{M,O_2} of 0.1546 cm s^{-1}, which is ~0.5% as large (or ~1/200) as the hypothetical P_{M,O_2} of Krogh's pure-water membrane. In other words, the RBC membrane offers substantial resistance to O_2 diffusion.

Each of the seven other labeled points corresponds to one other experimental condition. All points are shape corrected as detailed below, based on experimentally determined fractional decreases in k_{HbO2}, the measured or interpolated prevalence of nBCDs, and nBCD diameter. Note that the dKO and the WT+DIDS points nearly overlap.

Table 3 summarizes the key numerical values corresponding to the eight experimental points (to the left of the y-axis) in Figure 4. Note that the sum of % decrease in P_{M,O_2} for AQP1-KO (~21.6%) and RhAG-KO (~36.4%) is nearly equal to the P_{M,O_2} for the dKO (~55.2%). The largest % decrease in P_{M,O_2} occurs with dKO+pCMBS (~90.7%). The effects of the membrane-protein knockouts and inhibitors on P_{M,O_2}—along with the proteomics data in paper #2—supports the hypothesis that the vast majority of O_2 moves through channels in RBC plasma membrane: AQP1, Rh_{Cx}, and at least one additional channel that it blocked by pCMBS. In other words, "Overton's rule" applies, at most, to ~9% of the O_2 traffic across the murine RBC membrane.

Predicted dependence of O_2 offloading (k_{HbO2}) effect of decreased O_2 permeability of RBC membrane (P_{M,O_2}) on kinetic parameters

In Figure 2, we examined the $[O_2]_{Free}$, $[HbO_2]_i$, $[Hb]_i$, and HbSat time courses that our model predicts for a control (drug-free) WT RBC. In Figure 5, we extend this analysis of the WT-control condition (green) by adding two additional parameters—the total intracellular O_2 concentration ($[O_2]_{Free}$+$[HbO_2]$) and the O_2 efflux across the plasma membrane (J_{M,O_2}). In addition, we simulate the slowest O_2 offloading protocol observed in paper #1: a dKO RBC pre-treated with pCMBS (purple).

On the time scale of Figure 5*A*, the initial rate of decline for $[O_2]_{Free}$ appears to be nearly the same for dKO+pCMBS and WT-control. The difference in time courses becomes more evident after a few tens of milliseconds, as $[O_2]_{Free}$ rapidly falls to ~0 for the WT, whereas it remains elevated for dKO+pCMBS.

For $[HbO_2]$ in Figure 5*B*, the time courses are easily distinguishable from an early time.

The time courses of $[O_2]_{Free}$ + $[HbO_2]$ in Figure 5*C* are nearly the same as for $[HbO_2]$ alone in Figure 5*B*.

The time courses of HbSat in Figure 5*D*, when appropriately scaled, are nearly the same as for $[HbO_2]$ in Figure 5*B*. The reason is that, throughout the experiment, an overwhelming fraction of O_2 is bound to Hb as HbO_2 (even though the fraction is less at low $[O_2]_{Free}$, reflecting the shape of the HbO_2 dissociation curve).

Because the sum [Hb] + $[HbO_2]$ is constant, the time courses of [Hb] in Figure 5*E* is the inverse of $[HbO_2]$ in Figure 5*B*.

Finally, in Figure 5*F*, J_{M,O_2} is initially ~10-fold higher for WT-control than for dKO+pCMBS, reflecting the 91% decrease in P_{M,O_2} in the latter case. For WT-control, J_{M,O_2} rapidly plummets.

Mathematical simulations exploring the predicted sensitivity of k_{HbO2} to eight key kinetic and geometric parameters

To understand better the dependence of O_2 offloading on a range of parameters in Table 1, we performed a sensitivity analysis, studying eight key parameters. See Figure 1 for an overview of the model. Our approach was to start with the parameter values in Table 1; that is, with the provisional value P_{M,O_2} = 0.15 cm s^{-1}, our simulation yields the provisional MMM-k_{HbO2} = 3.99 s^{-1}. Next, as described in the following sections, we systematically varied, one at a time, each of the following: $k_{HbO2\rightarrow Hb}$ in Figure 6, $[Hbtot]_i$ in Figure 7, each of four diffusion constants in Figure 8*A–D*, ℓ_{EUF} in Figure 9, and $Ø_{Sphere}$ in Figure 10.

In each of these figures or panels, we plot MMM-k_{HbO2} on the y-axis and the varied parameter (as a % of the standard parameter value) on the x-axis. Thus, when the standard parameter value = 100%, MMM-k_{HbO2} = 3.99 s^{-1}. Also in each figure/panel, we present eight dashed horizontal lines, one for each of the experimental conditions. These are coded with an open or filled circle that ranges from a high MMM-k_{HbO2} = 3.99 s^{-1} for WT-control (0% decrease) to ~0.9% s^{-1} for dKO+pCMBS (78% decrease in MMM-k_{HbO2}).

$k_{HbO2\rightarrow Hb}$ *(governing reaction* $HbO_2 \rightarrow Hb + O_2$*)*

Figure 6 shows the dependence of MMM-k_{HbO2} on $k_{HbO2\rightarrow Hb}$. Understandably, when $k_{HbO2\rightarrow Hb}$ is zero, O_2 offloading comes to a halt and MMM-k_{HbO2} is zero as well. As $k_{HbO2\rightarrow Hb}$ rises, MMM-k_{HbO2} rises at first rapidly and then more slowly. The red dot represents the provisional control condition in which $k_{HbO2\rightarrow Hb}$ is 100% of the control value and MMM-k_{HbO2} is the familiar 3.99 s^{-1}. We see that that $k_{HbO2\rightarrow Hb}$ would have to fall by ~30% (i.e., x ≅ 70%) to account, by itself,

for even our smallest-observed decrease in SC-k_{HbO_2} = MMM-k_{HbO_2} (i.e., 3.73 s^{-1} for AQP1-KOs). In fact, the largest $k_{HbO_2 \rightarrow Hb}$ decrease observed in paper #1 was ~9%, and that was for dKO-control cells. In order for a decrease in $k_{HbO_2 \rightarrow Hb}$, by itself, to lower the observed SC-k_{HbO_2} to ~2.80 s^{-1} (horizontal purple dashed line), $k_{HbO_2 \rightarrow Hb}$ would have to have fallen by >60%. We conclude that the sensitivity of MMM-k_{HbO_2} to decreases in $k_{HbO_2 \rightarrow Hb}$ is too small have an appreciable impact on our O_2-offloading data.

[Hbtot]$_i$

Figure 7 shows the dependence of MMM-k_{HbO_2} on $[Hb_{tot}]_i$. Starting at x = 50% of the control value, increases in $[Hb_{tot}]_i$ cause MMM-k_{HbO_2} to fall at first steeply and then more shallowly. The reasons for this slowing of O_2 offloading are two-fold: (1) O_2 diffuses through the RBC far more slowly when part of the large HbO_2 tetramer than when free as O_2 and (2) as $[Hb_{tot}]_i$ increases, total O_2 increases—although $[O_2]_{Free}$ does not—meaning that more time is required to rid the cell of O_2.

In our experiments, MCHC tended to fall in the KOs, with the greatest decrease being ~8% in the RhAG-KOs (see paper #2). Thus, by themselves these decreases in MCHC (analogous to $[Hb_{tot}]_i$) would have caused an increase, rather than the observed decrease in SC-k_{HbO_2}. However, as noted in paper #2, the decreases in MCHC were accompanied by increases in MCV, which have the opposite effect on SC-k_{HbO_2} (as we will see below). Thus, the MCHC and MCV effects tend to cancel.

Diffusion constants

Figure 8 shows the dependence of MMM-k_{HbO_2} on the four relevant diffusion constants, namely, D for extracellular O_2 (the only relevant extracellular solute), and the three intracellular diffusion constants for the components of the equilibrium $HbO_2 \rightleftharpoons Hb + O_2$.

Extracellular D_{O_2}. Figure 8*A* shows that, starting from our standard extracellular value for D_{O_2} (i.e., 1.3313×10^{-5} cm^{2}s^{-1}; see Table 1)—indicated by the red dot—decreasing $(D_{O_2})_o$ at first has little effect, and then causes MMM-k_{HbO2} to fall steeply. However, $(D_{O_2})_o$—which almost certainly does not vary substantially with genotype—would have to fall by >30% to account for the fall in SC-k_{HbO2} in our AQP1-KO experiments, and by >60% to account for the dKO data.

Because $(D_{O_2})_o$ governs the abili ty of O_2 to diffuse through the EUF, away from the membrane surface to the bECF (where $[O_2] = 0$ to mimic the annihilation of O_2 by NDT), we are not surprised that MMM-k_{HbO2} approaches zero as $(D_{O_2})_o$ approaches zero. Thus, if $(D_{O_2})_o$ were zero, O_2 offloading would stop as soon as $[O_2]$ at the outer surface of the membrane rose to match $[O_2]_i$.

Note that our model does not explicitly take into account the diffusion of NDT from the bECF into the EUF. Although the diffusion constant for $S_2O_4^{=}$ is doubtlessly lower than that for O_2, $[S_2O_4^{=}]_{bECF}$ is ~71-fold greater than the initial $[O_2]_i$. Thus, we expect the EUF to be flooded with $S_2O_4^{=}$ very early in the physiological experiment. It is for this reason that others believe that ℓ_{EUF} is probably <1 μm, which, if true, means that $(D_{O_2})_o$ is even less impactful than indicated in Figure 8*A*.

Intracellular D_{O_2}. Figure 8*B* shows that the dependence of MMM-k_{HbO2} on $(D_{O_2})_i$ is similar to that of $(D_{O_2})_o$ in Figure 8*A*. In fact, starting from the red dot in Figure 8*B*, which represents our standard intracellular D_{O_2} (i.e., 2.7745×10^{-6} cm^2 s^{-1}; see Table 1), decreasing $(D_{O_2})_i$ causes MMM-k_{HbO2} to fall even less steeply than does decreasing $(D_{O_2})_i$. Thus, $(D_{O_2})_i$—which again we regard as unlikely to change substantially with genotype—would need to fall by >40% to account for the fall in SC-k_{HbO2} in our AQP1-KO experiments, and by nearly 80% to account for the dKO data.

Note that, as noted in Methods, our choice of $(D_{O_2})_i$ is already, historically, a rather low value. If $(D_{O_2})_i$ is in fact greater than we estimated, then the red dot would slide further to the right (i.e., on an even flatter part of the curve, then the MMM-k_{HbO2} would be even less sensitive to changes in $(D_{O_2})_i$.

Intracellular D_{HbO_2}. Figure 8*C* shows that MMM-k_{HbO2} is nearly insensitive to changes in D_{HbO_2} until, starting at the red dot, this parameter falls to a tiny fraction of its standard value (i.e., 6.07×10^{-8} cm^2 s^{-1}; see Table 1). The reason is that the diffusion constant of tetrameric HbO_2 (red dot) is so low that—even though the concentration of is high—the movement of HbO_2 per se toward the membrane during O_2 offloading has little effect on O_2 delivery, and thus to MMM-k_{HbO2}. Of course, in Figure 7 we saw that decreases in $[Hbtot]_i$ can greatly increase MMM-k_{HbO2}. The reason is that Hb acts as a near-stationary buffer that binds O_2 and nearly immobilizes it until O_2 release from HbO_2 permits the now-free O_2 to resume its net diffusion to the membrane or the next unoccupied Hb. Thus, we expect genotype-dependent changes in D_{HbO_2} to have only miniscule effects on SC-k_{HbO2} until D_{HbO_2} becomes so small that HbO_2 approaches absolute immobility.

Intracellular D_{Hb}. Figure 8*D* shows that MMM-k_{HbO2} is even less sensitive to changes in D_{Hb} than to D_{HbO_2}. The reasons are: (1) The diffusion constant for the deoxygenated Hb tetramer (i.e., 6.07×10^{-8} cm^2 s^{-1}; see Table 1) is nearly as low as it is for the fully oxygenated tetramer. And (2) Hb is moving away from the membrane during O_2 offloading. Thus, even if D_{Hb} were zero, the empty tetramers would pile up—at least mathematically—at the inner surface of the membrane, still maintaining a gradient for HbO_2 tetramers to diffuse toward the membrane. At $D_{Hb} = 0$, the small decrease in MMM-k_{HbO2} would reflect absent diffusion of Hb into the depth of the cytosol, and thus decreased formation of new HbO_2.

ℓ_{EUF}

Figure 9 shows that MMM-k_{HbO_2} has only weak dependence on ℓ_{EUF}. Starting at x = 100% of the control value (i.e., ℓ_{EUF} = 1 μm), decreasing ℓ_{EUF} to as low as 90% of control (i.e., 0.1 μm) could raise SC-k_{HbO_2} by <25%. Could an increase in ℓ_{EUF} account for our KO data? By itself, a 3× increase in ℓ_{EUF} would be needed to replicate the SC-k_{HbO_2} decrease that we see with AQP1-KOs, and a 10× to 20× increase would be needed to replicate the RhAG-KO. No amount of ℓ_{EUF} increase, alone, could account for our other data.

$Ø_{Sphere}$

The main part of Figure 10 and its inset (at a greatly reduced y-axis scale) show that MMM-k_{HbO_2} is quite sensitive to changes in the diameter of the equivalent sphere. The reason, of course, is the impact of diffusion distance. Even a ~50% increase in $Ø_{Sphere}$, by itself, would decrease MMM-k_{HbO_2} enough to mimic the effect of either a dKO or AQP1+DIDS. On the other hand, the curve flattens at higher $Ø_{Sphere}$, so that one would have to invoke a nearly 2.5× increase to account for the dKO+DIDS data, and nearly 4× to account for the dKO+pCMBS results. On the other hand, data from imaging flow cytometry shows that, among genotypes, (1) $Ø_{Major}$ falls by a maximum of only ~4% (i.e., from WT to RhAG-KO; see Table 2, data row 2), (2) MCV data from automated hematology rises by a maximum of only ~6.5% (i.e., from WT to RhAG-KO; see Table 2, data row 1), and (3) computed $Ø_{Sphere}$ rises by a maximum of only ~8% (i.e., from WT to RhAG-KO; see Table 2, data row 5).

Accommodation for non-BCDs

The inputs to the MMM simulation include four observed experimental parameters: (1) MCV and (2) MCH (from which we compute MCHC) both come from automated hematology; (3) $Ø_{Major}$ comes from imaging flow cytometry; and $k_{HbO_2 \rightarrow Hb+O_2}$ comes from stopped-flow absorbance spectroscopy on lysed RBCs. These values reflect all cells in the blood sample. An additional input

is an estimate of P_{M,O_2}. The output of the simulation is k_{HbO2}. Because the blood comprises both the dominant biconcave disks (BCDs) and minority non-BCDs (nBCDs), the paired values P_{M,O_2} (input) and k_{HbO2} (output) represent hybrid values that to some extent conflate BCDs and nBCDs. Our goal in this section is to obtain a $P_{M,O_2}/k_{HbO2}$ pair that estimates as accurately as possible the values for BCDs.

nBCD prevalence

Table 4 is an expanded version of Table 3. The first row of Table 4 lists the prevalence of nBCDs from paper #2[5]. The values for WT/Ctrl and dKO/Ctrl are around 2%, and may overestimate the actual values in SF experiments because of the extra time needed to prepare the samples for IFC analyses. The nBCD prevalence values for the AQP1-KO and RhAG-KO groups are interpolations of the WT/Ctrl and dKO/Ctrl values. The nBCD prevalence values are ~6-fold higher for the WT/pCMBS cells than the corresponding WT/Ctrl cells. The dKO/pCMBS values are only ~2-fold greater than the corresponding dKO/Ctrl cells, probably reflecting the partial absence of pCMBS targets after the elimination of AQP1 and Rh_{Cx}. The largest nBCD prevalence comes with WT/DIDS cells, at ~41%; the figure falls to ~21% in the dKO/DIDS group. These large percentages probably reflect the long incubation with DIDS (1 hour), compounded—as noted above—by the extra time needed (compared to SF experiments) for execute the IFC studies.

Provisional estimates of P_{M,O_2} and MMM-k_{HbO2}

As noted in Methods, we chose our provisional P_{M,O_2} for WT/Ctrl cells (Table 4, data row 2) to match the P_{CO_2} value of 0.15 cm s^{-1} that Endeward et al (Endeward *et al.*, 2006) obtained for the membrane CO_2 permeability of human RBCs. MMM simulations based on P_{M,O_2} = 0.15 cm

[5] See Paper #2

s^{-1} yield a provisional MMM-k_{HbO2} of 3.99 s^{-1} (row 3), a value that is rather close to the highest of the three hemolysis-corrected (HC) stopped-flow values (i.e., ~4.05 s^{-1}) for WT/Ctrl cells (see paper #1[6]).

For the seven columns to the right of "WT/Ctrl" in Table 4, we chose the provisional P_{M,O_2} values in iterative processes in which each P_{M,O_2} generated a corresponding provisional MMM-k_{HbO2} that approximately matched the experimental HC-k_{HbO2} value. Note that all $P_{M,O_2}/k_{HbO2}$ pairs lie on the sigmoid k_{HbO2} vs. log(P_{M,O_2}) curve in Figure 4.

In the next several sections, we present a novel, 2-step approach for deconvoluting the HC-k_{HbO2} data on a mixture of BCDs and nBCDs to extract an estimate the k_{HbO_2} of BCDs, and thereby arrive at a P_{M,O_2} that we assume to apply to both BCDs and nBCDs.

Using WT/Ctrl cells to illustrate our approach, we begin by making the (incorrect) assumption that the provisional MMM-k_{HbO2} of ~3.99 s^{-1} (Table 4, row 3) represents only BCDs (row 4, same as row 3). This allows us to construct an idealized time course of oxyhemoglobin (HbO_2) desaturation for BCDs (Figure 11*A*, green curve/furthest to the left). In parallel, knowing the measured $Ø_{Major}$ of nBCDs, and assuming them to be spheres with the same P_{M,O_2} as the BCDs (i.e., 0.15 cm s^{-1}), we construct another idealized desaturation time course, but this time for nBCDs (Figure 11*A*, blue curve/furthest to the right). We then linearly combine these two curves in proportion to the prevalence of their respective cells. Because the weighting is ~98.59% BCD and 1.41% nBCD, the mixture curve (Figure 11*A*, black) lies just to the right of the green BCD curve.

Figure 11*B* depicts a similar analysis for dKO/pCMBS cells. Here, reflecting the low P_{M,O_2}, all three curves show a slower offloading of O_2 from RBCs than in Figure 11*A*. Moreover, because

---

[6] See Paper #1

the nBCD prevalence is ~4-fold higher than for the WT/Ctrl cells in Figure 11*A*, the separation between the green (BCDs) and black (mixture) is more discernable.

Rebalancing of k_{HbO2} values

Note that in row 6 of Table 4, k_{HbO2} for the mixture is only ~3.95 s^{-1}, which is ~1% lower than our provisional estimate (~3.99 s^{-1}). The goal of the present step is to rebalance the three k_{HbO2} values so that the value for the mixture matches the original provisional k_{HbO2} as closely as possible. We make two assumptions:

- The term (MMM-$k_{\mathrm{HbO2/Mixture}}$ – MMM-$k_{\mathrm{HbO2/BCDs}}$)/(MMM-$k_{\mathrm{HbO2/BCDs}}$)) is maintained from the first linear combination through the rebalancing. That is, the rebalanced MMM-$k_{\mathrm{HbO2/BCDs}}$ exceeds the rebalanced MMM-$k_{\mathrm{HbO2/Mixture}}$ by the same fraction (~1.02% for WT/Ctrl) as it did during the first linear-combination step.
- The ratio (MMM-$k_{\mathrm{HbO2/nBCDs}}$)/(MMM-$k_{\mathrm{HbO2/BCDs}}$) remains similarly fixed from the first linear combination through the rebalancing. For WT/Ctrl, this is ~45.9%.

These provisos ensure that, after rebalancing, MMM-$k_{\mathrm{HbO2/Mixture}}$ is the same, within rounding errors, as our original provisional k_{HbO2}, which, after all, really encompassed both BCDs and nBCDs. Thus, after rebalancing, MMM-$k_{\mathrm{HbO2/BCDs}}$ is slightly elevated (~4.0358 s^{-1} for WT/Ctrl). Achieving this higher k_{HbO2} requires that our corresponding rebalanced $P_{\mathrm{M,O_2}}$ be increased from the provisional value—our next step.

Rebalancing P_{M,O_2} values

Armed with the rebalanced MMM-k_{HbO2} (~4.04 s^{-1} for WT/Ctrl in Table 4), we compute the rebalanced $P_{\mathrm{M,O_2}}$ from an inverted/linearized version of Figure 4, shown in Figure 12. The result in the case of WT/Ctrl is a value (~0.155 cm s^{-1}) that is only slightly higher than our provisional $P_{\mathrm{M,O_2}}$ of 0.15 cm s^{-1}.

Shape-correction factor ($\mathcal{F}_{SC}$)

For a given data genotype/treatment, $\mathcal{F}_{SC}$ is the ratio (rebalanced MMM-k_{HbO_2})/(provisional MMM-k_{HbO_2}), ~1.0102 in the case of WT/Ctrl cells. Multiplying an HC-k_{HbO_2} value (~4.05 s^{-1} for the first set of WT/Ctrl data) by $\mathcal{F}_{SC}$ yields an estimate of the shape-corrected (SC) k_{HbO_2} (~4.09 s^{-1} in this example). For dKO/pCMBS cells, with a higher nBCD prevalence than WT/Ctrl cells, $\mathcal{F}_{SC}$ is correspondingly higher, ~1.0376.

The remainder of Table 4, following the $\mathcal{F}_{SC}$ values, shows five sets of reference values (HC-k_{HbO_2} and SC-k_{HbO_2}). The first set pertains to three sets of control experiments: AQP1-KO/Ctrl, RhAG-KO/Ctrl, and dKO/Ctrl. The second set pertains to WT/pCMBS; the third, to WT/DIDS. The fourth and fifth sets are reference values for dKO/pCMBS and dKO/DIDS, respectively.

The last two rows of Table 4 show the percent decreases in HC-k_{HbO_2} and SC-k_{HbO_2}, based on shape-corrected values, for each genotype/treatment, relative to WT/Ctrl. These are the same values listed above in Table 4.

Discussion

To test whether the observed decreases in k_{HbO2} correspond to decreases in $P_{M,O2}$ and to provide estimates of $P_{M,O2}$ from measured k_{HbO2} values, we developed a three-dimensional reaction-diffusion model of O_2 efflux from an RBC. In this model, we simplify the RBC by assuming that it is a perfectly symmetric sphere, the diameter of which equals the computed thickness of an RBC.

The model describes how the concentrations of O_2, HbO_2 and Hb change in time and space, when O_2 diffuses out of the cytosol, across the plasma membrane, throughout the EUF and finally to the bECF. For our initial estimate of P_{M,O_2} in our mathematical simulations, we assume that P_{M,O_2} in mouse RBCs has the same value as measured by Endeward *et al.* (2006*b*) for the CO_2 permeability of human RBCs.

Despite our mathematical model being relatively simple and based only on first principles, our assumptions as well as the physiological data that inform the model are sufficient to have a computational model that makes physiological meaningful predictions for a WT mouse. One strength of this study is the use of the genotype-specific flow cytometry and hematology data generated in the present studies to establish parameter values.

Krogh-Erlang equation

In his pioneering modeling work on O_2 delivery from capillary to tissue (Krogh, 1919) August Krogh introduced a now-famous equation—derived by his mathematician-colleague Mr. K Erlang—that played a major role in elucidating the fundamental principles of how $[O_2]$ changes both longitudinally along the capillary and radially away from it. This equation reflects a highly simplified view of the system, which of course was necessary at that time, given the limitations in available computational algorithms and computing power. The analysis by Kreuzer (1982) lists 15 assumption—some of which he and others had noted previously—that are implicit in the derivation

of the Krogh-Erlang equation. Assumption #12 states that "the diffusion coefficient [of O_2] is the same throughout the tissue." Assumption #7 (previously noted by Hess (Hess, 1930))—really a corollary of #12—states that "the capillary wall does not present any resistance to oxygen diffusion." Another corollary of #12 is that no cell membrane, including that of the RBC, offers resistance to O_2 diffusion. We examine implications of this implicit assumption in the section below.

How others concluded that the plasma membrane offers no resistance to O_2 diffusion

After Krogh's landmark paper, most practitioners in the field firmly adopted this implicit assumption. However, a series of studies from Roughton and his colleagues led to the suggestion that the plasma membrane of RBCs offers significant resistance to the movement of gases, including CO_2 and O_2 (Blank & Roughton, 1960; Gibson *et al.*, 1955; Forster, 1964; Roughton, 1964; Nicolson & Roughton, 1951). However, later studies questioned this possibility and attributed the observed resistance to the extracellular unconvected layer (UL) of fluid that surrounds the cells after flow stops in the SF apparatus (Kutchai, 1975; Coin & Olson, 1979; Huxley & Kutchai, 1981; Vandegriff & Olson, 1984*b*; Holland *et al.*, 1985; Hughes & Bates, 2003). It is true that studies that focus on O_2 influx across RBCs are intrinsically challenging because this influx depletes O_2 at the surface of the RBC, and the UL of that surrounds the RBC offers resistance to the replenishment of O_2 from the bECF (Coin & Olson, 1979; Huxley & Kutchai, 1981; Holland *et al.*, 1985; Hughes & Bates, 2003). Moreover, as pointed out by Vandegriff and Olson, the low solubility of O_2 in water enhances the effect of ULs in experiments of O_2 influx (Vandegriff & Olson, 1984*b*). Nevertheless, it is possible that the implicit assumption of past authors—namely, that the plasma membrane offers no resistance of O_2 diffusion (R_{Membrane})—may have led them to dismiss Roughton hypothesis prematurely. The total resistance (R_{Total}) to O_2 diffusion from Hb to bECF is the sum of the effective resistance of the intracellular

fluid (R_{ICF}), $R_{Membrane}$, and the resistance of the extracellular unconvected fluid (R_{EUF}). If one implicitly assumes that $R_{Membrane} \cong 0$, the result is that the sum ($R_{Membrane} + R_{EUF}$) reduces to R_{EUF}, with the result that one computes erroneously high values for the EUF thickness. In the process, one concludes that the large UL explains the experimental data without the need of invoking membrane resistance—a classic bootstrap maneuver.

Because Vandegriff and Olson recognized the challenge of studying O_2 influx, these authors investigated the role of the plasma membrane in the movement of O_2 in the case of O_2 efflux. They reduced the effects of ULs by adding large amounts of sodium dithionite (NaDT) in the suspending medium (Vandegriff & Olson, 1984*b*) .The NaDT near the outer side of the plasma membrane annihilates the O_2 that has just left the RBC, thereby minimizing the build-up of O_2 and minimizing the UL. Viewed somewhat differently, the NaDT maximizes the outwardly directed O_2 gradient and therefore the rate of O_2 efflux (Holland *et al.*, 1985). Vandegriff and Olson used a reaction-diffusion model of an RBC, idealized as a cylindrical disk, to analyze the time course of their O_2 release data. They concluded that their mathematical model—which lacked a term analysis to $R_{Membrane}$—could simulate their data without the need to include a membrane resistance to the movement of O_2. Instead, they accounted for their O_2-release data in the presence of NaDT in the extracellular medium by including in the model an UL, the width of which increased with time from the initial value of 1 μm to ~30 μm (computed from an equation in ref. (Holland *et al.*, 1985)). In summary, because they implicitly assumed $R_{Membrane} = 0$, these authors invoked a very large R_{EUF}, and used this result to conclude that $R_{Membrane} \cong 0$.

It is worth noting that at least 3 sets of authors have performed physicochemical experiments in which they concluded that lipid mono/bilayers can offer substantial resistance to CO_2 or O_2 (Blank & Roughton, 1960; Strutwolf *et al.*, 2001; Ivanov *et al.*, 2004).

Recent observations on D_{O_2} in the cytosol of RBCs

In their 2020 paper, Richardson et al conclude that the D_{O_2} in the cytosol of RBCs is far lower than previously thought (Richardson *et al.*, 2020). The generally accepted value for D_{O_2} in RBC cytosol has been 5.09×10^{-6} cm^2/ s^{-1} at 10 °C (Clark *et al.*, 1985), which is ~38% of the value in water (i.e., 13.313×10^{-6} cm^2 s^{-1} at 10 °C). However, Richardson et al conclude that the actual D_{O_2} value in RBC cytosol is <0.7×10^{-6} cm^2 s^{-1} at 23 °C, which is < ~3.5% of the value in water at 23 °C (i.e., 20×10^{-6} cm^2 s^{-1}). In other words, Richardson et al conclude that D_{O_2} value that others have been using for RBC cytosol is a great overestimate.

Calculation of D_{O_2} by Richardson et al. In SI of their paper (page 6), these authors report a value of 2500 μm^2 s^{-1} (i.e., 2.5×10^{-5} cm^2 s^{-1}) for D_{O2} in water at 23 °C. In the main text of their paper (page 3), these authors—based on physiological data and their mathematical simulations—infer that D_{O2} in RBC cytosol is <70 μm^2 s^{-1}. They report this as <5% of the D_{O2} in water (in fact, the factor is <3.5%; see above). However, in the original reference (Han & Bartels, 1996) that Richardson et al cited for D_{O2} in water, Han and Bartels (Han & Bartels, 1996) report the value of 2500 μm^2 s^{-1} for D_{O2} in water at ~35 °C, not at the temperature of 23 °C, used in the Richardson experiments. According to Han and Bartels, the value of D_{O2} in water at ~23 °C should be ~2000 μm^2 s^{-1}. Thus, the D_{O_2} in cytoplasm predicted by Richardson et al should be 70/2000 = 1/29 of that in water rather than 70/2500 = 1/36.

To compare our work to that of Richardson et al, we must recompute their D_{O_2} for a temperature of 10 °C. As noted above, Han and Bartels report that D_{O2} in water at 10 °C is 1.3313 $\times 10^{-5}$ cm^2 s^{-1} (Han & Bartels, 1996). If we divide this figure by 29, we arrive at a predicted value of D_{O_2} (based on the work of Richardson et al) of $(1.3313 \times 10^{-5})/29 = 4.5907 \times 10^{-7}$ cm^2 s^{-1}..

Our calculation of the D_{O_2} of RBC cytosol (excluding membrane) at 10 °C. As discussed in the main text of our paper, we believe that this D_{O_2} value of 4.5907×10^{-7} cm^2 s^{-1} is excessively

high because Richardson et al used a $[NDT]_o$ of only 1 mM, rather than the final concentration in the present study, 25 mM. Several groups—Coin and Olson(Coin & Olson, 1979) , Vandegriff and Olson (Vandegriff & Olson, 1984*b*) , and Holland et al. (Holland *et al.*, 1985)—have emphasized the importance of employing a sufficiently high $[NDT]_o$ to minimize the EUF layer. Thus, using an $[NDT]_o$ of only 1 mM, Richardson et al would have attributed to the ICF a component of total resistance ($R_{Total} = R_{ICF} + R_{Membrane} + R_{EUF}$) really due to the EUF layer. Recognizing that the value of Richardson et al is an overestimate, we decided to average the Richardson value of 0.45907×10^{-6} cm^2 s^{-1} with the generally accepted value (Clark *et al.*, 1985) of 5.09×10^{-6} cm^2 s^{-1}. Thus, we assumed that D_{O_2} in RBC cytoplasm is 2.7745×10^{-6} cm^2 s^{-1}.

Contribution of channels to D_{O_2} of the cytosol + membrane. Richardson et al argue that the D_{O_2} of the cytosol (actually, the cytosol + membrane) is far lower than previously believed. We argue that they overestimate this effect. Nevertheless, the reason that D_{O_2} (of the cytosol + membrane) is as high as it is, is because of the presence of O_2 channels. If one were to eliminate ~90% of these channels—as by genetically deleting AQP1 and RhAG, while applying pCMBS—the membrane would now dominate R_{Total}.

Importance of values used in modeling

Thickness of EUF (ℓ_{EUF})

Despite the use of NaDT in our SF experiments—which virtually abolishes the formation of ULs (Holland *et al.*, 1985)—in our mathematical model we made the conservative assumption that the EUF has a thickness of 1 μm and that no NaDT is present in this layer. We simulated the annihilation of O_2 by NaDT by assuming that the bECF contains no O_2 during the duration of the simulations. In Figure 9 we examined the dependence of k_{HbO2} on ℓ_{EUF}. When we increase ℓ_{EUF}, the simulated k_{HbO_2} asymptotically falls to a value that approximates the biological value that we observe with RBCs from a dKO mouse. Thus, no increase in ℓ_{EUF} can account for our data with

pCMBS or DIDS. Lowering ℓ_{EUF} to values smaller than 1 μm causes steep increases in the simulated k_{HbO2} (i.e., decreases in the resistance of the EUF to O_2 diffusion, R_{EUF}). Starting from such elevated k_{HbO_2} values, the model can generate lower k_{HbO_2} values by increasing $R_{Membrane}$, that is, by decreasing the permeability of the plasma membrane to O_2 (P_{M,O_2}) so that the sum (R_{EUF} + $R_{Membrane}$) remains the same. In other words, if the UL is thinner than 1 μm—which is likely to be the case in the presence of high [NaDT]—the membrane must make a greater contribution to the overall diffusive resistance of O_2.

Calculation of the contribution of the plasma membrane to total diffusive resistance to O_2

Let us assume that we can treat the diffusion of O_2 from the ICF of the RBC to the bECF like an electrical circuit (see Figure 1*A*). Thus, the total resistance to diffusion (R_{Total}) is the sum of the resistance of the ICF (R_{ICF}), the plasma membrane ($R_{Membrane}$), and the EUF (R_{EUF}):

$$R_{Total} = R_{ICF} + R_{Membrane} + R_{EUF}$$

In the next 3 sections, we will compute each of the resistances on the right side of the equation, and then we will compute the fraction of R_{Total} that $R_{Membrane}$ represents. See Table 1 for parameter values used in simulations of RBCs from WT mice.

Calculate R_{ICF}. We start by computing—at the time t_{37} (i.e., 0.2760 s), when hemoglobin saturation (HbSat) has fallen to 1/e of its initial value—the parallel fluxes of free O_2 (J_{O_2}) and HbO_2 (J_{HbO_2}) from the position of the average O_2 and HbO_2 molecules in the ICF. From these two fluxes, we then compute the total O_2 flux (J_{TO_2}).

First, we determine the number of O_2 molecules in each of the 101 shells (i = 1 to 101) that make up the model RBC, as well as the distance (ℓ) from the center of each shell to the inner surface of the plasma membrane (iPM). For a WT cell with no inhibitors, we find that the average

distance of an O_2 molecule from the iPM is 2.792×10^{-5} cm. For HbO_2, a similar analysis yields an average distance of 2.560×10^{-5} cm. Because these distances are so similar, we used the average distance for O_2 and HbO_2, which is 2.68×10^{-5} cm, which corresponds to shell $i = k = 76$ from the center of the sphere. We call this average distance ℓ_k. Thus, the O_2 flux from ℓ_k to the iPM is:

$$J_{O_2} = \frac{D_{O_2}}{\ell_k}\cdot\left([O_2]_k - [O_2]_{iPM}\right) = 0.000540\,\mu\text{mole}/(\text{cm}^2\,\text{s}),$$

where D_{O_2} is the diffusion constant for O_2 in the ICF (see Table 1 for value), and where $[O_2]_k$ = 0.01528 mM and $[O_2]_{iPM}$ = 0.01007 mM at t_{37}. For HbO_2,

$$J_{HbO_2} = \frac{D_{HbO_2}}{\ell_k}\cdot\left([HbO_2]_k - [HbO_2]_{iPM}\right) = 0.000282\,\mu\text{mole}/(\text{cm}^2\,\text{s}),$$

where D_{HbO_2} is the diffusion constant for HbO_2 in the ICF (see Table 1 for value), and where $[HbO_2]_k$ = 6.869 mM and $[HbO_2]_{iPM}$ = 6.744 mM at t_{37}.

Thus, the total O_2 flux from ℓ_k to the iPM is

$$J_{TO_2} = J_{O_2} + J_{HbO_2} = 0.0008218\,\mu\text{mole}/(\text{cm}^2\,\text{s}).$$

The effective resistance to the diffusion of O_2 is

$$R_{ICF} = \frac{\ell_k}{D_{O_2}} = \frac{\left([O_2]_k - [O_2]_{iPM}\right)}{J_{TO_2}} = 6.334\ \text{s}\cdot\text{cm}^{-1}.$$

Calculate $R_{Membrane}$. We calculate the resistance of the plasma membrane to O_2 diffusion as the reciprocal of the "true" microscopic permeability of the plasma membrane to O_2 (P_{M,O_2}), which is 0.15 cm s^{-1} (see Table 1 for value). Thus,

$$R_{Membrane} = \frac{1}{P_{M,O_2}} = 6.666\ \text{s}\cdot\text{cm}^{-1}.$$

Calculate R_{EUF}. We calculate the resistance of the EUF to O_2 diffusion as

$$R_{\mathrm{EUF}} = \frac{\ell_{\mathrm{EUF}}}{D_{\mathrm{O_2}}} = 7.511\ \mathrm{s \cdot cm^{-1}},$$

where ℓ_{EUF} is the thickness of the EUF and D_{O_2} is the diffusion constant for O_2 in the EUF (see Table 1 for values).

Compute the contribution of $R_{Membrane}$ to R_{Total}. We calculate the contribution of $R_{Membrane}$ to R_{Total} the EUF as

$$\text{Contribution of } R_{\mathrm{PM}} \text{ to } R_{\mathrm{Total}} = \frac{R_{\mathrm{Membrane}}}{R_{\mathrm{Total}}} = \frac{R_{\mathrm{Membrane}}}{R_{\mathrm{ICF}} + R_{\mathrm{Membrane}} + R_{\mathrm{EUF}}}$$
$$\frac{6.666\ \mathrm{s \cdot cm^{-1}}}{6.334\ \mathrm{s \cdot cm^{-1}} + 6.666\ \mathrm{s \cdot cm^{-1}} + 7.511\ \mathrm{s \cdot cm^{-1}}} = 32.5\%.$$

Note that if ℓ_{EUF} is in fact <1 μm (i.e., R_{EUF} < 7.511 s cm^{-1}), the contribution of $R_{Membrane}$ to total resistance would be greater than ~32.5%.

Recalling that $R_{Total} = R_{ICF} + R_{Membrane} + R_{EUF}$, what do the present data tell us about the contribution of $R_{Membrane}$ and O_2 channels to R_{Total}? R_{ICF} is doubtlessly important, as emphasized recently by Richardson and colleagues (Richardson *et al.*, 2020). However, their low $[NDT]_o$ of 1 mM (vs. our value of 25 mM) likely leads to a large effective ℓ_{EUF} for O_2 and thus an overestimated R_{ICF} (Coin & Olson, 1979; Vandegriff & Olson, 1984*b*; Holland *et al.*, 1985). In our simulations, we have assumed that the intracellular diffusion constant for O_2 (D_{i,O_2}) is the arithmetic mean of the generally accepted value and the lower Richardson value. Our simulations reveal that $R_{Membrane}$—even for WT RBCs without inhibitors—is ~33% of R_{Total}. To the extent that our estimates of R_{ICF} (from D_{i,O_2}) and R_{EUF} (from ℓ_{EUF}) are too high, as is likely true, the contribution of the membrane to the slowing of O_2-offloading is still higher. Thus, even for control RBCs from WT mice, the membrane offers substantial resistance to O_2 diffusion, contrary to Krogh's implicit

assumption. Moreover, $R_{Membrane}$ would be even higher if it were not for the normal complement of O_2 channels. Our mathematical simulations reveal the steep predicted dependence of k_{HbO_2} on P_{M,O_2} (Figure 4) or, viewed differently, how fractional decreases in P_{M,O_2} lead to fractional decreases in k_{HbO_2}. Thus, the 30% decrease in k_{HbO_2} caused by the dKO corresponds to a ~55% decrease in P_{M,O_2}, so that $R_{Membrane}$ now represents nearly half of R_{Total}. The 78% decrease in k_{HbO_2} caused by dKO+pCMBS corresponds to a ~91% decrease in P_{M,O_2}, so that $R_{Membrane}$ now represents ~83% of R_{Total}—even with our conservative estimates of R_{ICF} (i.e., D_{i,O_2}) and R_{EUF} (i.e., ℓ_{EUF}). It is not clear how drugs confined to the outside of the membrane or deletion of membrane proteins could produce the observed decreases of k_{HbO_2} in any way other than decreasing O_2 egress through protein channels. Moreover, an analysis of 8 key parameters (e.g., ℓ_{EUF}, cell thickness) based on mathematical simulations shows that no reasonable change in any could explain our k_{HbO_2} data (Figure 6 through Figure 10).

Acknowledgements

We thank Jean-Pierre Cartron for the gift of *Rhag*–/– mice, and for most helpful discussions. We thank Seong-Ki Lee for developing an improved approach for genotyping the *Rhag*–/– mice. The authors gratefully acknowledge Daniela Calvetti and Erkki Somersalo for having developed the engine of an earlier version of the CO_2/pH reaction-diffusion model of an oocyte, which in part served as the starting point for the RBC model. We also thank Thomas Radford for organizing the husbandry of the mouse colonies; Gerald Babcock for his role as laboratory manager. This work was supported by Office of Naval Research (ONR) grant N00014-11-1-0889, N00014-14-1-0716, and N00014-15-1-2060; a Multidisciplinary University Research Initiative (MURI) grant N00014-16-1-2535 from the DoD, NIH grant multi-scale modeling grant 5U01GM111251 (to WFB), and NIH grant R01HL160857 (to WFB). R.O. and the modeling were supported in part by NIH grant K01-DK107787. W.F.B. gratefully acknowledges the support of the Myers/Scarpa endowed chair.

Tables

Table 1. Parameter values used in mathematical simulations of RBCs from WT mice

		Bulk ECF	Plasma membrane	Bulk ICF	Reference
Physical constants					
Temperature (°C)		10		10	Paper #1
P_{H_2O}, Vapor pressure of H_2O (mmHg)				9.2	From Forstner & Gnaiger (1983)
Literature values					
P_{50}, P_{O_2} of half-maximal hemoglobin saturation curve (mmHg)				9.35	From Roughton *et al.* (1936)
O_2 solubility (mM/mmHg)				2.24×10^{-3}	From Forstner & Gnaiger (1983)
Hill coefficient				2.7	From ref. (Popel, 1989)
Assumptions					
P_{M,O_2}, O_2 permeability (cm/s)			0.15		Assumed same as CO_2 permeability in RBCs (Endeward *et al.*, 2006)
ℓ_{EUF}, Thickness of EUF (μm)		1.0			
Thickness of membrane (nm)			5		
Shell thickness (cm or μm)		10^{-6} or 10^{-2}		10^{-6} or 10^{-2}	
Calculated values					
$Ø_{Sphere}$, Sphere diameter (cm or μm)				2.02×10^{-4} or 2.02	See Methods
D, Diffusion coefficient (cm^2/sec)	O_2	1.3313×10^{-5}			Computed using data from ref. (Han & Bartels, 1996)
				2.7745×10^{-6}	See Discussion

	Hb	0		6.07×10^{-8}	Computed using data from ref. (Clark *et al.*, 1985)
	HbO_2	0		6.07×10^{-8}	Computed using data from ref. (Clark *et al.*, 1985)
Hb/HbO_2 reaction					
Rate constants (sec^{-1})	$k_{HbO2 \rightarrow Hb}$			11.60	Measured
(mM^{-1} sec^{-1})	$k_{Hb \rightarrow HbO2}$			6.7481×10^4 ($k_{Hb \rightarrow HbO2}$ varies with $[O_2]$; this is initial value)	Computed using Eqn 4 in Methods
Equilibrium constant (mM)	K			1.1790×10^{-4} (K varies with $k_{Hb \rightarrow HbO2}$; this is initial value)	Calculated as ($k_{HbO2 \rightarrow Hb}$/ $k_{Hb \rightarrow HbO2}$)
Concentration (mM)	Total Hb	0		18.73	See Methods
	O_2	0		0.3532 (21% O_2)	Computed from O_2 solubility (above), using Henry's law
	HbO_2 monomer	0		18.6767	Computed using the relation $[HbO_2] = [Hb]_{tot} ([O_2]^n/(K+[O_2]^n)$
	Hb monomer	0		0.0533 mM	Computed as $[Hb]_{tot} - [HbO_2]$

Parameter values correspond to the experimental temperature of 10°C.

Table 2. Genotype-specific parameter values used in mathematical simulations of RBCs in Figure 3

Parameter \ Mouse	WT	AQP1-KO	RhAG-KO	dKO	Reference
MCV (fl)	47.9	49.5	51.0	49.8	From paper #2
$Ø_{Major}$, major diameter of RBC (μm)	6.80	6.69	6.53	6.55	From paper #2 (We assume that $OD_{Torus} = Ø_{Major}$)
***r*, minor radius of torus (μm)**	1.01	1.04	1.09	1.07	Computed from Eqn (5)
***R*, major radius of torus (μm)**	2.39	2.31	2.18	2.21	$R = (OD_{Torus})/2 - r$ Torus volume (computed from *r* & *R*) = MCV *R* & r are computed such that torus volume = MCV
$Ø_{Sphere}$, diameter of equivalent sphere (μm)	2.02	2.08	2.18	2.14	$Ø_{Sphere} = 2 \times r$
MCH, mean corpuscular hemoglobin (pg)	14.4	14.1	14.7	14.5	From paper #2
MCHC, mean corpuscular hemoglobin concentration (g/dl)	30.1	28.6	28.7	29.4	From paper #2 MCHC = MCH/MCV
$[\text{Total Hb monomers}]_i$ (mM)	18.73	17.71	17.87	18.16	See Methods/HbContent
Initial $[HbO_2 \text{ monomers}]_i$ (mM)	18.6767	17.6596	17.8191	18.1083	Computed using the relation $[HbO_2] = [Hb]_{tot} ([O_2]^n/(K+[O_2]^n)$
Initial $[\text{Hb monomers}]_i$ (mM)	0.0533	0.0504	0.0509	0.0517	Computed as $[Hb]_{tot} - [HbO_2]$

*Values not listed here, but necessary for the mathematical simulations, are in Table 1, which also repeats four values in the "WT" column of this table (i.e., ØSphere, [Total Hb monomers]i, Initial [HbO2 monomers]i, Initial [Hb monomers]i). dKO, double knockout (i.e., genotype Aqp1–/–Rhag–/–). The parameters in Table 2 that establish the genotype-specific conditions for each simulation are: (1) the RBC thickness, which we compute from the measured ØMajor and MCV, and (2) the total Hb concentration, which we compute from measured MCV and MCH. Thus, the input parameters for the four simulations that mimic RBCs from WT, AQP1-KO, RhAG-KO and dKO mice are all the same (including PM,O2) with the exception of the RBC thickness and total Hb concentration, which are specific to each mouse genotype.

Table 3. Parameter values predicted by macroscopic mathematical modeling

Parameter \ Protocol	WT/ Ctrl	AQP1-KO	RhAG-KO	dKO/ Ctrl	WT/ pCMBS	WT/ DIDS	dKO/ pCMBS	dKO/ DIDS
SC-P_{M,O_2} (cm s^{-1})	0.1546	0.1213	0.0983	0.0693	0.0281	0.0673	0.0143	0.0376
SC-k_{HbO_2} (s^{-1})	4.0358	3.6828	3.3582	2.7988	1.5282	2.7533	0.8687	1.8937
↓ SC-P_{M,O_2} vs. WT/Ctrl	0%	21.56%	36.43%	55.20%	81.80%	56.47%	90.72%	75.71%
↓ SC-k_{HbO_2} vs. WT/Ctrl	0%	8.85%	16.53%	30.47%	61.24%	31.25%	77.70%	52.98%

The SC-P_{M,O_2} (via the MMM) yields the SC-k_{HbO_2}.

Ctrl, control conditions (i.e., no DIDS or pCMBS); MMM, macroscopic mathematical model; SC, shape corrected.

Table 4. Detailed parameter values predicted by macroscopic mathematical modeling

Parameter \ Protocol	WT/ Ctrl	AQP1-KO	RhAG-KO	dKO/ Ctrl	WT/ pCMBS	WT/ DIDS	dKO/ pCMBS	dKO/ DIDS
nBCD prevalence	1.41%	1.96%	1.96%	2.51%	8.71%	41.03%	5.72%	21.27%
Provisional P_{M,O_2} (cm s^{-1})	0.15	0.1175	0.0957	0.0673	0.0261	0.0417	0.0137	0.0309
Provisional MMM-k_{HbO_2} (s^{-1})	3.9949	3.6338	3.3146	2.7560	1.4388	2.0356	0.8372	1.6367
1st LC-k_{HbO_2} (s^{-1}), BCDs	3.9949	3.6338	3.3146	2.7560	1.4388	2.0356	0.8372	1.6367
1st LC-k_{HbO_2} (s^{-1}), nBCDs	1.8331	1.7489	1.6262	1.4390	0.6923	0.9697	0.4234	0.8058
1st LC-k_{HbO_2} (s^{-1}), mixture	3.9545	3.5855	3.2715	2.7138	1.3547	1.5050	0.8069	1.4146
Rebalanced MMM-k_{HbO_2} (s^{-1}), BCDs	4.0358	3.6828	3.3582	2.7988	1.5282	2.7533	0.8687	1.8937
Rebalanced MMM-k_{HbO_2} (s^{-1}), BCDs	1.8519	1.7725	1.6476	1.4614	0.7353	1.3116	0.4394	0.9324
Rebalanced MMM-k_{HbO_2} (s^{-1}), mixture	3.9949	3.6338	3.3146	2.7560	1.4388	2.0356	0.8372	1.6367
Rebalanced P_{M,O_2} (cm s^{-1}), all cells	0.1546	0.1213	0.0983	0.0693	0.0281	0.0673	0.0143	0.0376
$\mathcal{F}_{SC}$ (shape-correction factor)	1.0102	1.0135	1.0132	1.0155	1.0621	1.3526	1.0376	1.1570
HC-k_{HbO_2} (s^{-1}) from SF*	4.0457	3.6758	3.3670	2.7982	----	----	----	----
SC-k_{HbO_2} (s^{-1}) from SF*	4.0871	3.7253	3.4114	2.8417	----	----	----	----
HC-k_{HbO_2} (s^{-1}) from SF†	3.4197	----	----	----	1.2609	----	----	----
SC-k_{HbO_2} (s^{-1}) from SF†	3.4547	----	----	----	1.3392	----	----	----
HC-k_{HbO_2} (s^{-1}) from SF‡	3.2116	----	----	----	----	1.6491	----	----
SC-k_{HbO_2} (s^{-1}) from SF‡	3.2445	----	----	----	----	2.2306	----	----
HC-k_{HbO_2} (s^{-1}) from SF§	----	----	----	2.4779	----	----	----	1.4707
SC-k_{HbO_2} (s^{-1}) from SF§	----	----	----	2.5165	----	----	----	1.7017
HC-k_{HbO_2} (s^{-1}) from SF‖	----	----	----	2.5885	----	----	0.8126	----
SC-k_{HbO_2} (s^{-1}) from SF‖	----	----	----	2.6287	----	----	0.8432	----
↓ SC-P_{M,O_2} vs. WT/Ctrl	0%	21.56%	36.43%	55.20%	81.80%	56.47%	90.72%	75.71%
↓ SC-k_{HbO_2} vs. WT/Ctrl	0%	8.85%	16.53%	30.47%	61.24%	31.25%	77.70%#	52.98%¶

The “nBCD prevalence” values (from IFC) for AQP1-KO and RhAG-KO are interpolations of the WT/Ctrl and dKO/Ctrl values. The Provisional P_{M,O_2} (via the MMM) yields the Provisional MMM-k_{HbO2}; these two rows contain the same data as the first two rows of Table 3. The Rebalanced P_{M,O_2} yields the Rebalanced MMM-k_{HbO2}. $\mathcal{F}_{SC}$ is the quotient of (Rebalanced MMM-k_{HbO2})/(Provisional MMM-k_{HbO2}) in the same column.
LC, linear combination; MMM, macroscopic mathematical model; HC, hemolysis corrected; SC, shape corrected; SF, stopped flow; Ctrl, control conditions (i.e., no DIDS or pCMBS).

*WT/Ctrl in this row is the reference value for AQP1-KO, RhAG-KO, dKO; †WT/Ctrl in this row is the reference value for WT/pCMBS; ‡WT/Ctrl in this row is the reference value for WT/DIDS; §dKO/Ctrl in this row is the reference value for dKO/DIDS; ‖dKO/Ctrl in this row is the reference value for dKO/pCMBS; ¶Computed from % decreases in SC-k_{HbO2} for dKO/Ctrl vs. WT/Ctrl (i.e., 30.47%) and dKO/DIDS vs. matched dKO/Ctrl (i.e., 32.38%, not shown); #Computed from % decreases in SC-k_{HbO2} for dKO/Ctrl vs. WT/Ctrl (i.e., 30.47%) and dKO/DIDS vs. matched dKO/Ctrl (i.e., 67.92%, not shown).

Figure Legends

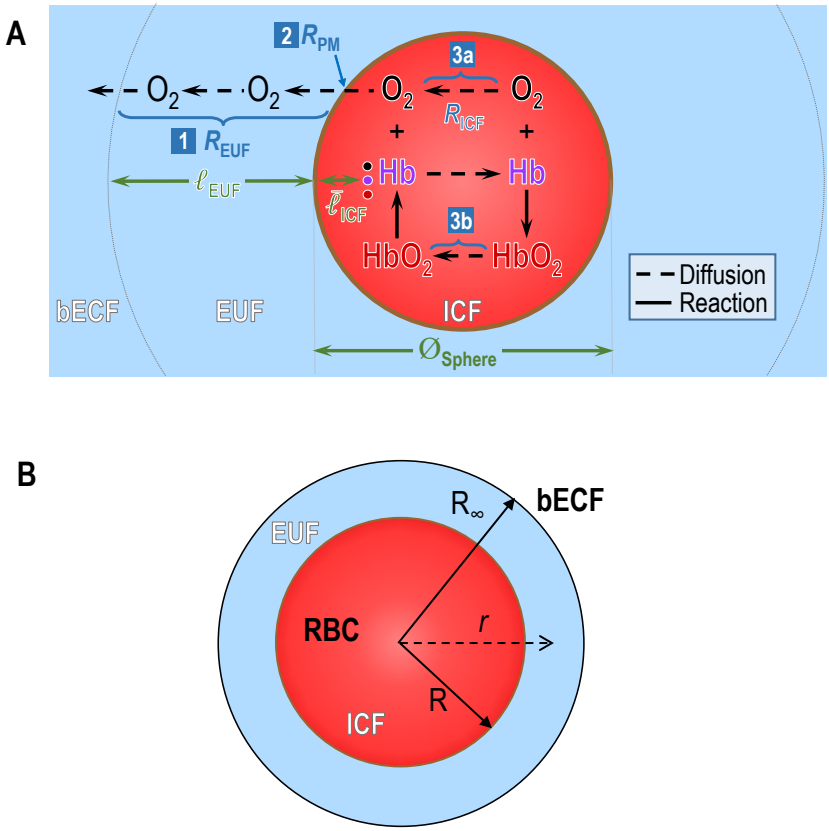

Figure 1. Mathematical model of O_2 efflux from an RBC

A, Major components of mathematical model of spherical RBC cell, the diameter of which matches the computed thickness of an average RBC from a WT or KO mouse. See text for details on the model.

B, The computational domain. For panel 'A', the abbreviations are: bECF, bulk extracellular fluid; EUF, extracellular unconvected fluid; ICF, intracellular fluid; PM, plasma membrane; $Ø_{Sphere}$, diameter of sphere (matches thickness of RBC); ℓ_{EUF}, thickness of EUF; 3 values of $\bar{\ell}_{ICF}$ are average distance from PM to the following 3 molecules in ICF: (a) O_2 (black dot and lettering), (b) Hb (violet), or HbO_2 (red) in ICF; [1] R_{EUF}, effective resistance offered by EUF to O_2 diffusion from PM to bECF; [2] R_{PM}, effective resistance offered by PM to O_2 diffusion; [3] R_{ICF}, effective resistance offered by ICF to combined diffusion of O_2 and HbO_2. $1/R_{ICF} = 1/R_{ICFa} + 1/R_{ICFb}$, where R_{ICFa} is effective resistance offered by ICF to O_2 diffusion over the distance $\bar{\ell}_{ICF}$, from the position of the average O_2 to PM; R_{ICFb} is effective resistance offered by ICF to HbO_2 diffusion over the distance $\bar{\ell}_{ICF}$, from the position of the average HbO_2 to PM. For panel 'B', the abbreviations are: R_∞, maximal radial distance from the center of the sphere ($R_\infty = R + \ell_{EUF}$); r, radial distance from the center of the cell.

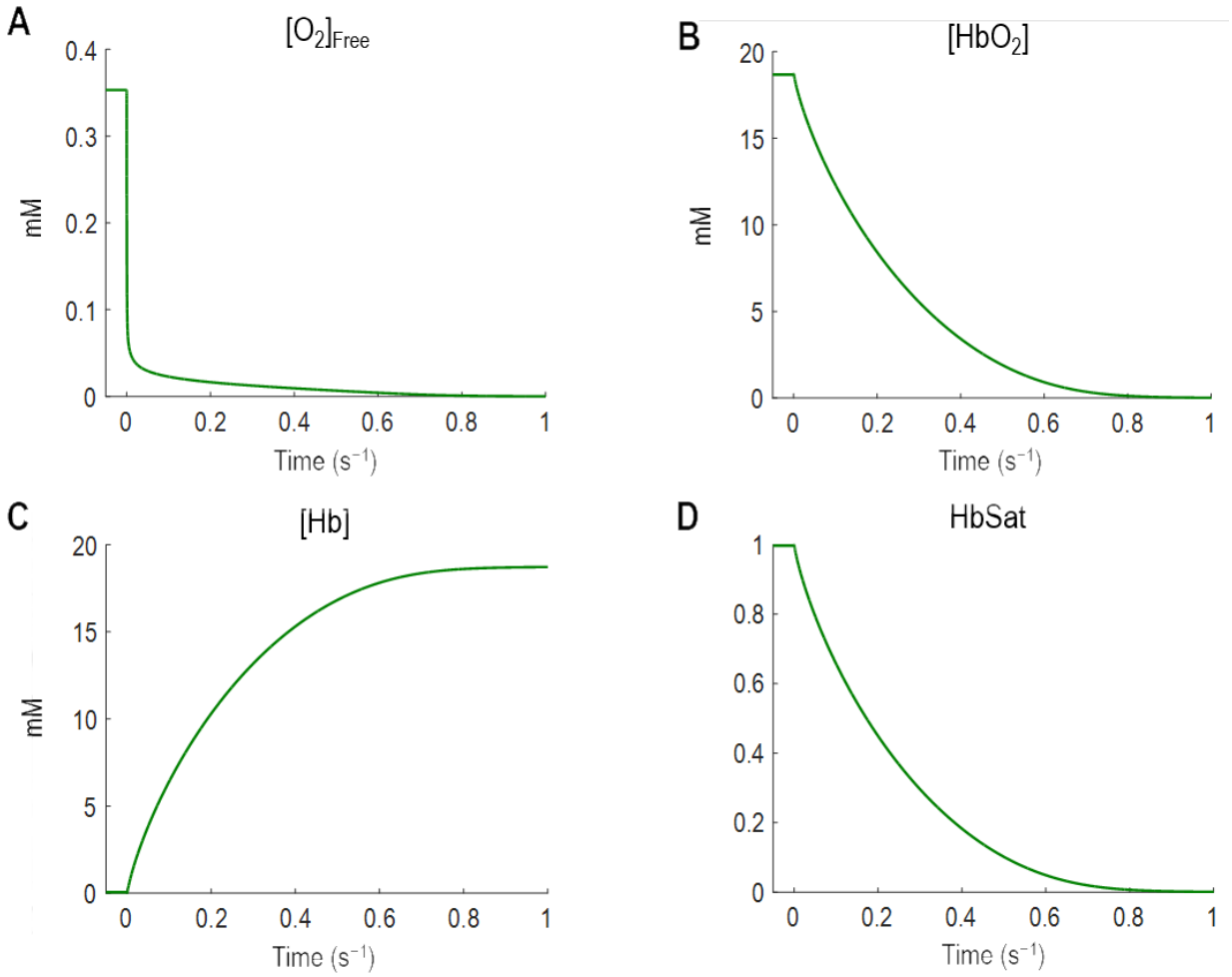

Figure 2. Simulated time courses of O_2/Hb-related parameters for cells mimicking WT/no inhibitors (control)

For this simulation, the input parameters are those reported in Table 1. See text for details on the model and simulations.

A, Concentration of free O_2, integrated over the entire volume of cytoplasm.

B, Concentration of oxyhemoglobin (HbO_2) monomers, integrated over the entire volume of cytoplasm.

C, Concentration of free hemoglobin (Hb), integrated over the entire volume of cytoplasm.

D, Hemoglobin saturation (HbSat) integrated over the entire volume of cytoplasm.

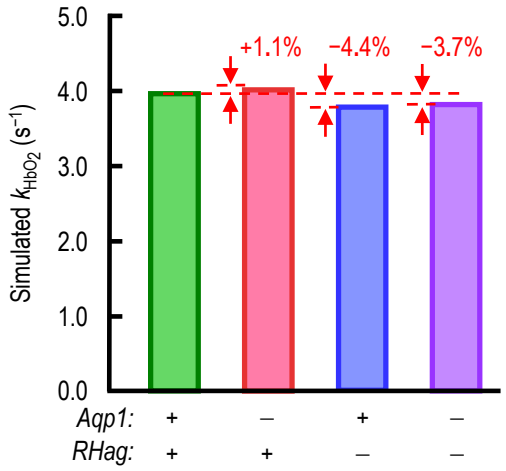

Figure 3. Predicted k_{HbO_2} values from simulations of RBCs from WT and KO mice.

Informed by hematological and morphological studies, which provide genotype-specific information on MCV, MCH, and $Ø_{Major}$ (see Table 2) we perform four simulations, one per genotype (WT, AQP1-KO, RhAG-KO, dKO), to test whether changes in MCV, MCH, and $Ø_{Major}$ can explain the decreases in hemolysis-corrected hc-k_{HbO_2} reported in paper #1. The model predicts that for (1) RBCs from *Aqp1*–/– mice, k_{HbO_2} should have increased by 1.1%, rather than decreased by ~9%, as observed; (2) RBCs from *Rhag*–/– mice, k_{HbO_2} should have decreased k_{HbO_2} by 4.4%, not the observed ~17%; and (3) RBCs from dKO mice, k_{HbO_2} should have decreased k_{HbO_2} by only 3.7%, not the observed ~30%. Thus, the hematological/morphological changes cannot explain our observed k_{HbO_2} data.

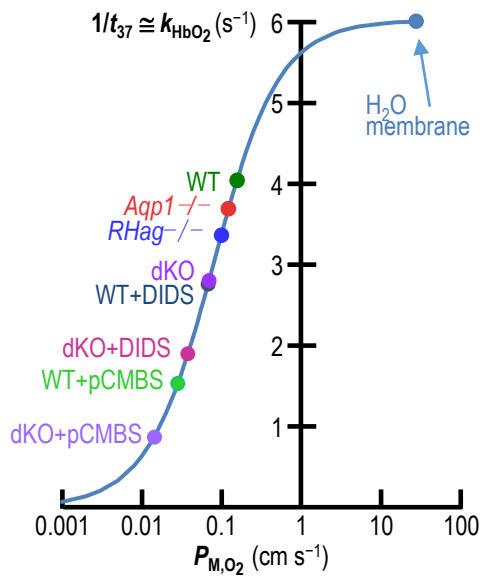

Figure 4. Predicted dependence of k_{HbO2} on P_{M,O_2}.

Predicted effects on hemolysis-corrected/shape-corrected k_{HbO_2} of varying P_{M,O_2} according to our reaction-diffusion model. See text for details on how we estimate P_{M,O_2} and then use this value to simulate k_{HbO_2} for normoshapen cells. To obtain the sigmoidal curve, we systematically vary P_{M,O_2} (x-axis) and use our mathematical model to compute k_{HbO_2} (y-axis). The point labeled WT has the coordinates (P_{M,O_2} = 0.1546 cm s^{-1}, k_{HbO_2} = 4.0358 s^{-1}). Note that the dKO and the WT+DIDS points nearly overlie each other. The point labeled "H_2O membrane" is the result of a simulation in which we assumed that the diffusion constant of O_2 in the plasma membrane is the same as in water.

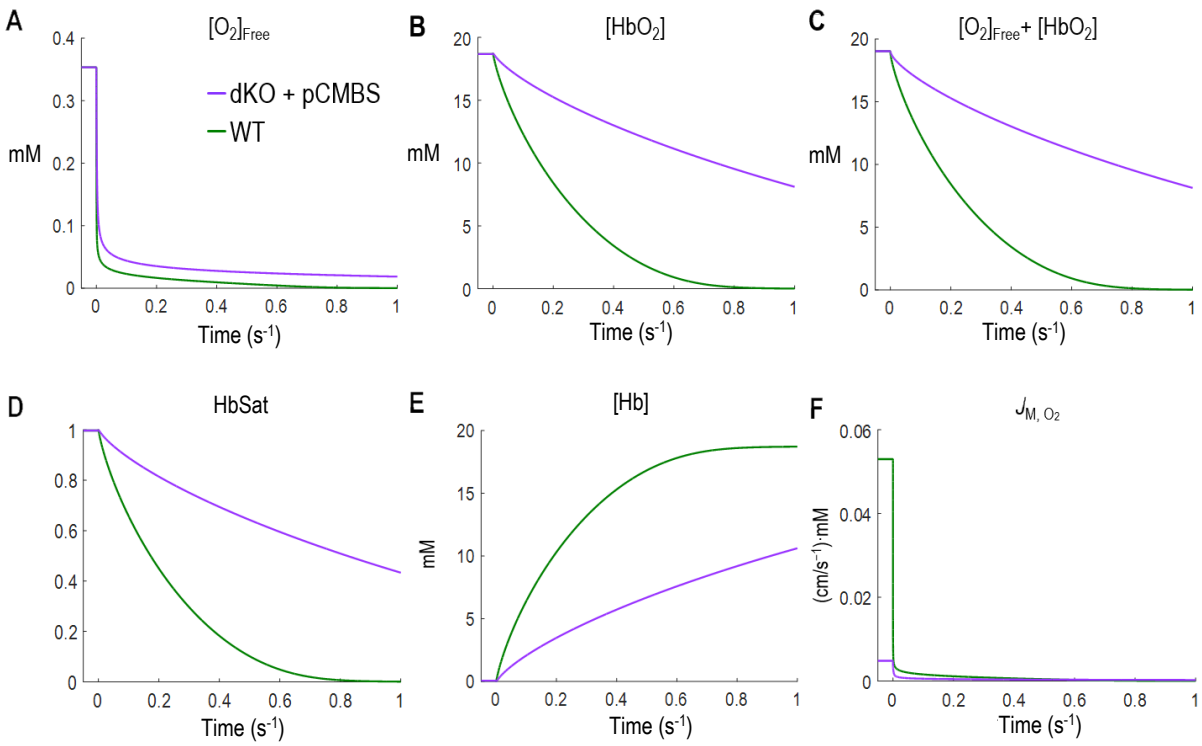

Figure 5. Simulated time courses of O_2/Hb-related parameters and transmembrane O_2 flux for cells mimicking WT/no inhibitors (control) vs. dKO+pCMBS.

We extend the analysis of the WT-control condition (green) shown in Figure 2 by adding two additional parameters—the total intracellular O_2 concentration ($[O_2]_{Free}$+$[HbO_2]$) and the O_2 efflux across the plasma membrane (J_{M,O_2}). In addition, we simulate the slowest O_2 offloading protocol observed in paper #1: a dKO RBC pre-treated with pCMBS (purple). See text for details on the model and simulations.

A, Concentration of free O_2, integrated over the entire volume of cytoplasm.

B, Concentration of oxyhemoglobin (HbO_2) monomers, integrated over the entire volume of cytoplasm.

C, Concentration of total O_2—sum of free O_2 and HbO_2 monomer—integrated over the entire volume of cytoplasm.

D, Hemoglobin saturation (HbSat) integrated over the entire volume of cytoplasm.

E, Concentration of free hemoglobin (Hb), integrated over the entire volume of cytoplasm.

F, Flux of O_2 across plasma membrane (J_{M,O_2}).

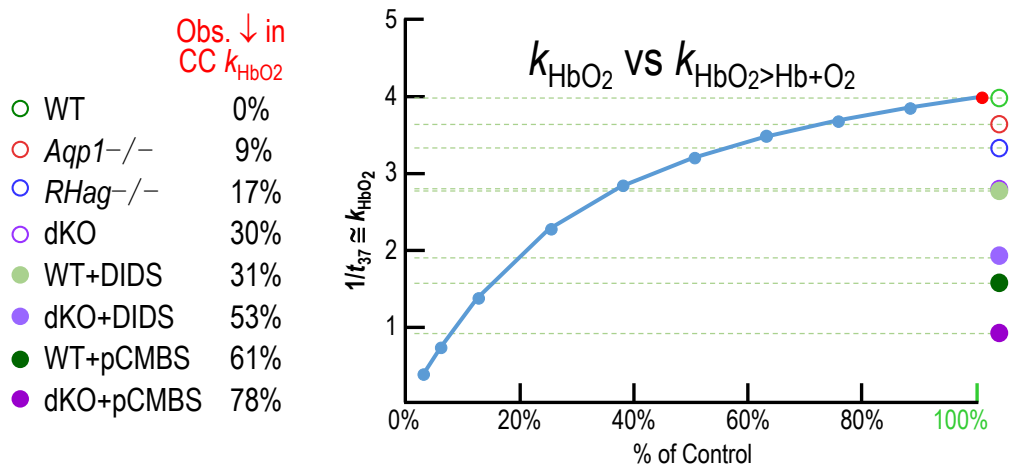

Figure 6. Mathematical simulations exploring the predicted sensitivity of k_{HbO_2} to changes in the rate constant of the reaction $HbO_2 \rightarrow Hb + O_2$.

Starting with the parameter values that generated the "WT" point in the first round of simulations, we performed nine additional simulations by systematically varying the rate constant ($k_{HbO_2>Hb}$) for deoxygenation of HbO_2: $HbO_2 \rightarrow Hb + O_2$, and computed k_{HbO_2}. The red dot—associated with 100% of $k_{HbO_2>Hb}$ (green text with green tick mark)—indicates the conditions for control RBCs (from WT mice, no inhibitors). The horizontal dashed lines indicate the k_{HbO_2} values, relative to control, for each of the other 7 experimental conditions. As summarized in the legend on the left, for each condition, we multiplied the control simulated k_{HbO_2} (i.e., 3.995 s^{-1}) by experimentally observed decrease in k_{HbO_2} (e.g., 8.85% for RBCs from *Aqp1*–/– mice) to obtain the simulated k_{HbO_2} for that condition (e.g., 3.641 s^{-1} for *Aqp1*–/– RBCs).

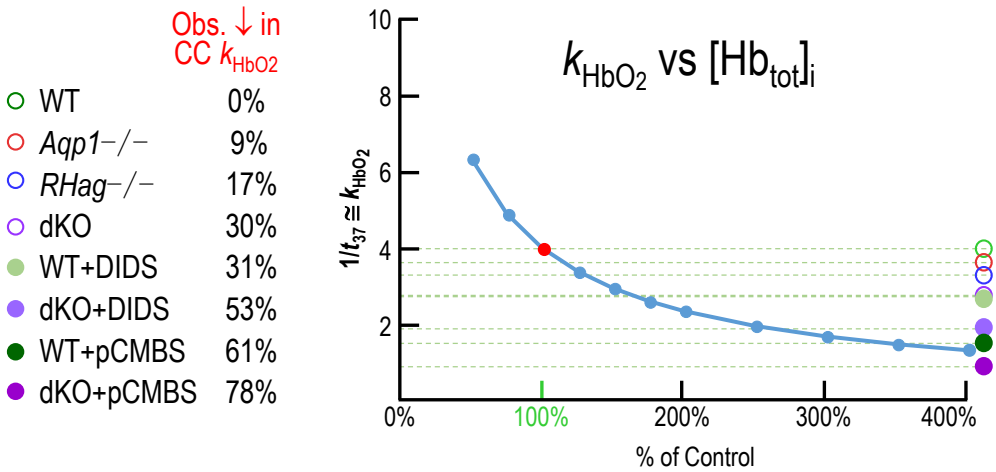

Figure 7. Mathematical simulations exploring the predicted sensitivity of k_{HbO_2} to changes in total intracellular Hb concentration.

Starting with the parameter values that generated the "WT" point in the first round of simulations, we performed ten additional simulations by systematically varying the total intracellular Hb concentration, $[Hb_{tot}]_i$, and computed k_{HbO_2}. The red dot—associated with 100% of $[Hb_{tot}]_i$ (green text with green tick mark)—indicates the conditions for control RBCs (from WT mice, no inhibitors). The horizontal dashed lines indicate the k_{HbO_2} values, relative to control, for each of the other 7 experimental conditions. As summarized in the legend on the left, for each condition, we multiplied the control simulated k_{HbO_2} (i.e., 3.995 s^{-1}) by experimentally observed decrease in k_{HbO_2} (e.g., 8.85% for RBCs from *Aqp1*–/– mice) to obtain the simulated k_{HbO_2} for that condition (e.g., 3.641 s^{-1} for *Aqp1*–/– RBCs). Only very large increases in $[Hb_{tot}]_i$ could explain our experimental data.

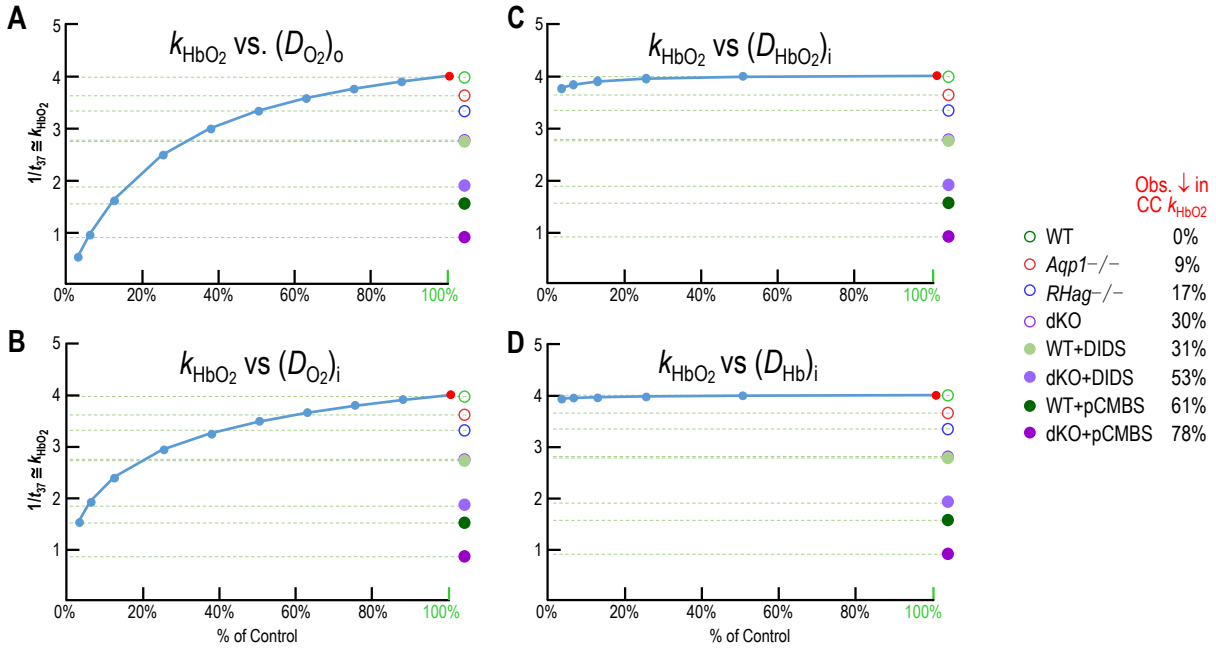

Figure 8. Mathematical simulations exploring the predicted sensitivity of k_{HbO_2} to changes in diffusion constants of solutes.

Starting with the parameter values that generated the "WT" point in the first round of simulations, we performed additional simulations by systematically varying four parameters, one at a time, and computed k_{HbO_2}. The red dot—associated with 100% of the value of the varied parameter (green text with green tick mark)—indicates the conditions for control RBCs (from WT mice, no inhibitors). The horizontal dashed lines indicate the k_{HbO_2} values, relative to control, for each of the other 7 experimental conditions. As summarized in the legend on the right, for each condition, we multiplied the control simulated k_{HbO_2} (i.e., 3.995 s^{-1}) by experimentally observed decrease in k_{HbO_2} (e.g., 8.85% for RBCs from *Aqp1*–/– mice) to obtain the simulated k_{HbO_2} for that condition (e.g., 3.641 s^{-1} for *Aqp1*–/– RBCs).

A, Dependence on diffusion constant for O_2 (D_{O_2}) in EUF—$(D_{O_2})_o$. Although this is one of the parameters to which k_{HbO_2} is most sensitive, it is also the one known with greatest confidence under control conditions, and the least subject to change with alterations in our experimental conditions.

B, Dependence on diffusion constant for O_2 (D_{O_2}) in ICF—$(D_{O_2})_i$. Only very large decreases in D_{O_2} could explain even our smallest experimental effect on k_{HbO_2} (i.e., *Aqp1*–/– RBCs).

C, Dependence on diffusion constant for oxy-Hb (D_{HbO_2}) in ICF—$(D_{HbO_2})_i$.

D, Dependence on diffusion constant for deoxy-Hb (D_{Hb}) in ICF—$(D_{Hb})_i$.

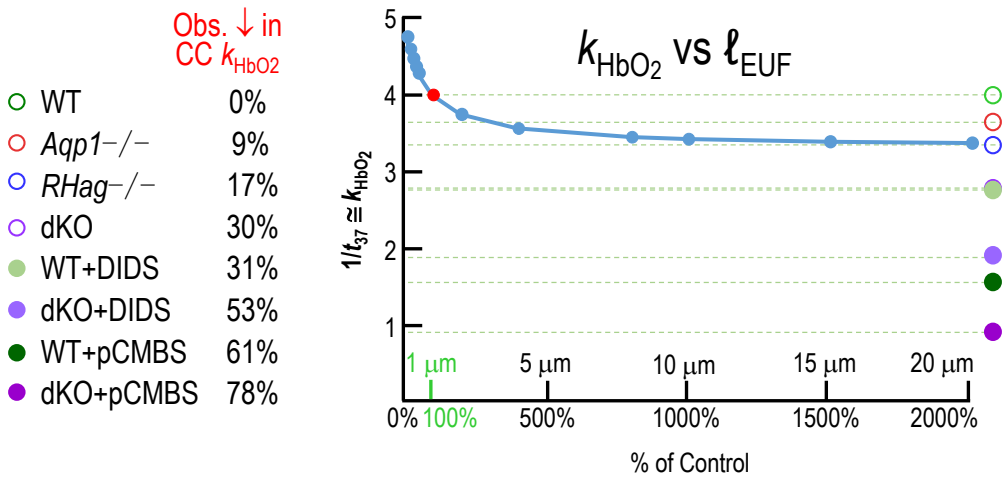

Figure 9. Mathematical simulations exploring the predicted sensitivity of k_{HbO_2} to changes in thickness of the EUF.

Starting with the parameter values that generated the "WT" point in the first round of simulations, we performed additional simulations by systematically varying the thickness of the EUF, ℓ_{EUF}, and computed k_{HbO_2}. The red dot—associated with 100% of ℓ_{EUF} (green text with green tick mark)—indicates the conditions for control RBCs (from WT mice, no inhibitors). The horizontal dashed lines indicate the k_{HbO_2} values, relative to control, for each of the other 7 experimental conditions. As summarized in the legend on the left, for each condition, we multiplied the control simulated k_{HbO_2} (i.e., 3.995 s^{-1}) by experimentally observed decrease in k_{HbO_2} (e.g., 8.85% for RBCs from *Aqp1*–/– mice) to obtain the simulated k_{HbO_2} for that condition (e.g., 3.641 s^{-1} for *Aqp1*–/– RBCs). Note that a near-tripling of ℓ_{EUF} would be necessary to account for the *Aqp1*–/–data, a ~20× increase would be necessary to account for the *Rhag*–/– data, and no amount of increase could—by itself—explain the other SC-k_{HbO_2} data.

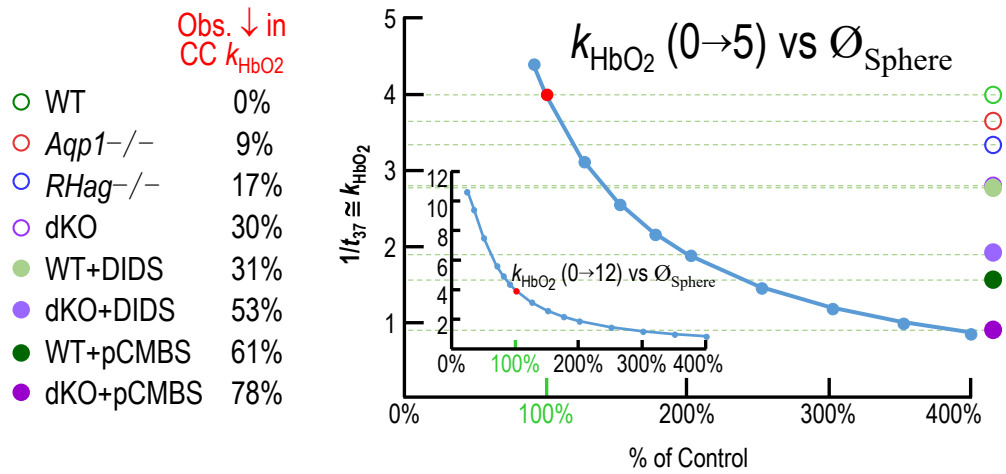

Figure 10. Mathematical simulations exploring the predicted sensitivity of k_{HbO_2} to changes in sphere diameter.

Starting with the parameter values that generated the "WT" point in the first round of simulations, we performed additional simulations by systematically varying the diameter of the sphere ($Ø_{Sphere}$) and computed k_{HbO_2}. The red dot—associated with 100% of $Ø_{Sphere}$ (green text with green tick mark)—indicates the conditions for control RBCs (from WT mice, no inhibitors). The horizontal dashed lines indicate the k_{HbO_2} values, relative to control, for each of the other 7 experimental conditions. As summarized in the legend on the left, for each condition, we multiplied the control simulated k_{HbO_2} (i.e., 3.995 s^{-1}) by experimentally observed decrease in k_{HbO_2} (e.g., 8.85% for RBCs from *Aqp1*–/– mice) to obtain the simulated k_{HbO_2} for that condition (e.g., 3.641 s^{-1} for *Aqp1*–/– RBCs). Note that main panel shows the y-axis from 0 to 5 s^{-1}, whereas the inset expands the y-axis to extend from 0 to 12 s^{-1}.

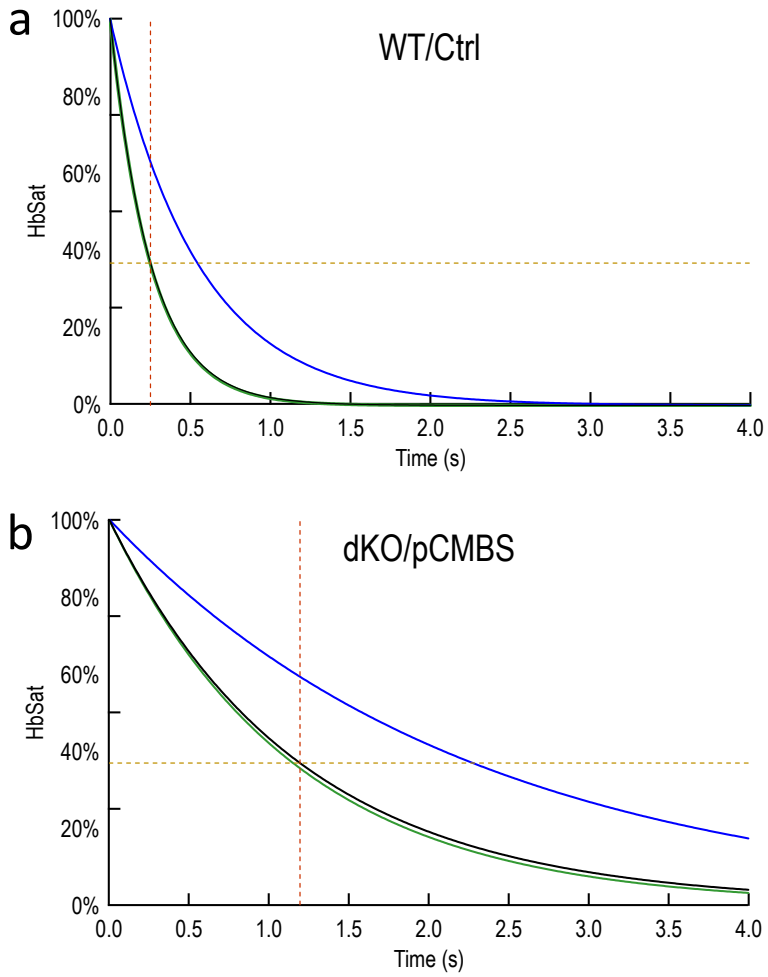

Figure 11. Initial linear-combination analysis of k_{HbO_2}

A, WT/Ctrl. The green curve is the computed decay of HbSat (hemoglobin saturation) for a biconcave disk (BCD). The blue curve is the computed decay for a non-BCD. The black curve, barely visible to the right of the green curve, is the linear combination of the green and blue curves, weighted for the respective prevalence of BCDs and nBCDs, respectively.

B, dKO/pCMBS. Similar to panel *A* except here the calculations are for a dKO cell treated with pCMBS.

The horizontal dashed lines represent 1/e. The vertical dashed line represent one time constant (τ).

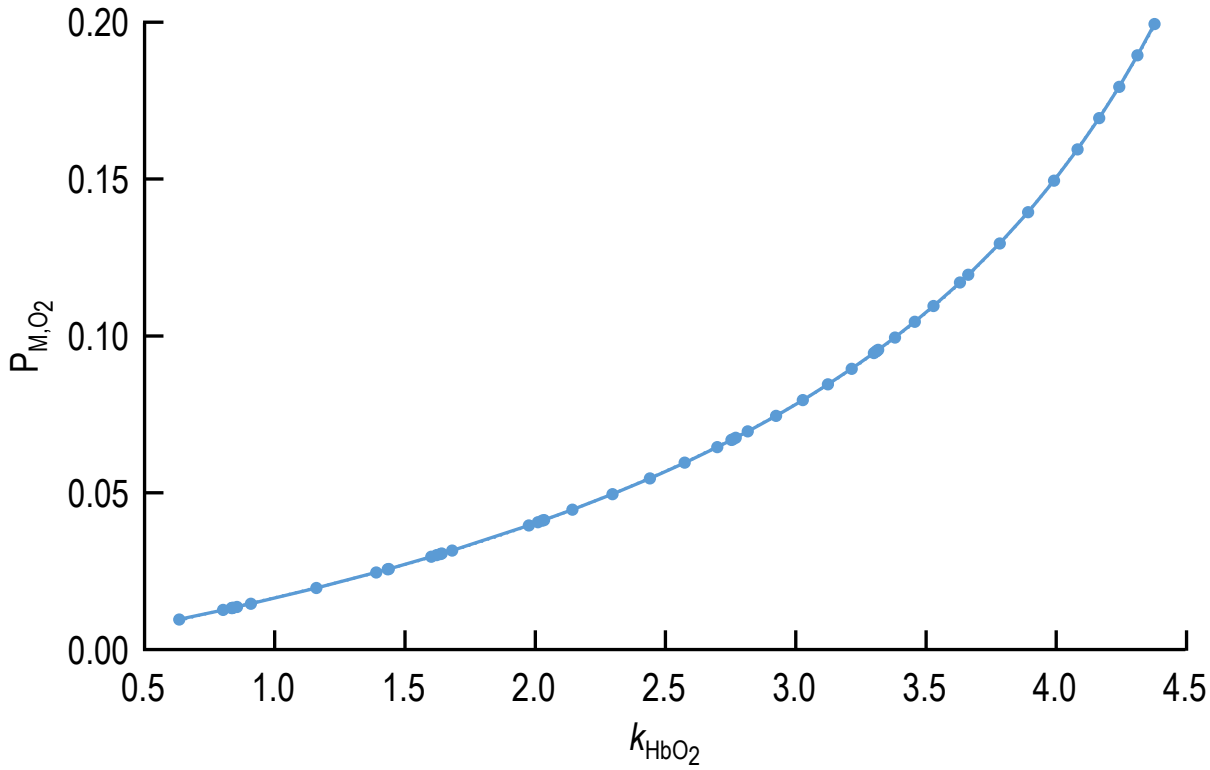

Figure 12. Inverted sigmoid plot

This figure is analogous to Figure 4 except that here we plot P_{M,O_2} on the y-axis, which is now linear, and k_{HbO2} on the x-axis. The displayed points are actual results of MMM calculations, and the upward-sloping curve is a trend line created from a 5th-order polynomial. This is a convenient tool for interpolating P_{M,O_2} values that correspond to a particular k_{HbO2} value as part of the rebalancing of P_{M,O_2}.

References

Adair GS, Bock AV & Field H (1925). The hemoglobin system VI. the oxygen dissociation curve of hemoglobin. *J Biol Chem* **63,** 529–545.

Blank M & Roughton FJW (1960). The permeability of monolayers to carbon dioxide. *Trans Faraday Soc* **56,** 1832–1841.

Boron WF (2010). Sharpey-Schafer lecture: gas channels. *Exp Physiol* **95,** 1107–1130.

Boron WF, Endeward V, Gros G, Musa-Aziz R & Pohl P (2011). Intrinsic CO_2 permeability of cell membranes and potential biological relevance of CO_2 channels. *ChemPhysChem* **12,** 1017–1019.

Clark A, Federspiel WJ, Clark PA & Cokelet GR (1985). Oxygen delivery from red cells. *Biophys J* **47,** 171–181.

Coin JT & Olson JS (1979). The rate of oxygen uptake by human red blood cells. *J Biol Chem* **254,** 1178–1190.

Cooper GJ & Boron WF (1998). Effect of pCMBS on CO_2 permeability of *Xenopus* oocytes expressing aquaporin 1 or its C189S mutant. *Am J Physiol* **275,** C1481-1486.

Cooper GJ, Occhipinti R & Boron WF (2015). CrossTalk proposal: Physiological CO_2 exchange can depend on membrane channels. *J Physiol*; DOI: 10.1113/JP270059.

Deonikar P, Abu-Soud HM & Kavdia M (2014). Computational analysis of nitric oxide biotransport to red blood cell in the presence of free hemoglobin and NO donor. *Microvasc Res* **95,** 15–25.

Deonikar P & Kavdia M (2013). Contribution of membrane permeability and unstirred layer diffusion to nitric oxide-red blood cell interaction. *J Theor Biol* **317,** 321–330.

Endeward V (2012). The rate of the deoxygenation reaction limits myoglobin- and hemoglobin-facilitated O_2 diffusion in cells. *J Appl Physiol* **112,** 1466–1473.

Endeward V, Al-Samir S, Itel F & Gros G (2014). How does carbon dioxide permeate cell membranes? A discussion of concepts, results and methods. *Front Physiol* **4,** 382.

Endeward V, Musa-Aziz R, Cooper GJ, Chen L-M, Pelletier MF, Virkki LV, Supuran CT, King LS, Boron WF & Gros G (2006). Evidence that aquaporin 1 is a major pathway for CO_2 transport across the human erythrocyte membrane. *FASEB J* **20,** 1974–1981.

Fick A (1855). V. On liquid diffusion. *Lond Edinb Dubl Phil Mag* **10,** 30–39.

Forster RE (1964). Rate of gas uptake by red cells. In *Handbook of Physiology*, pp. 827–837. American Physiological Society.

Forstner H & Gnaiger E (1983). Appendix A. Calculation of equilibrium oxygen concentration. In *Polarographic oxygen sensors: aquatic and physiological applications*. Springer-Verlag, Berlin Heidelberg New York.

Geers C & Gros G (2000). Carbon dioxide transport and carbonic anhydrase in blood and muscle. *Physiol Rev* **80,** 681–715.

Gibson QH, Kreuzer F, Meda E & Roughton FJ (1955). The kinetics of human haemoglobin in solution and in the red cell at 37 degrees C. *J Physiol (Lond)* **129,** 65–89.

Graham T (1829). Notice of the singular inflation of a bladder. *Quart J Sci* **II,** 88–89.

Graham T (1833). XXVII. On the law of the diffusion of gases. *Lond Edinb Dubl Phil Mag* **2,** 175–190.

Han P & Bartels DM (1996). Temperature Dependence of Oxygen Diffusion in H_2O and D_2O. *J Phys Chem* **100,** 5597–5602.

Hartridge H & Roughton FJ (1927). The rate of distribution of dissolved gases between the red blood corpuscle and its fluid environment: Part I. Preliminary experiments on the rate of uptake of oxygen and carbon monoxide by sheep's corpuscles. *J Physiol (Lond)* **62,** 232–242.

Hess WR (1930). *Die regulierung des Blutkreislaufes: gleichzeitig ein Beitrag zur Physiologie des vegetativen Nervensystemes*. Thieme.

Holland RA, Shibata H, Scheid P & Piiper J (1985). Kinetics of O_2 uptake and release by red cells in stopped-flow apparatus: effects of unstirred layer. *Respir Physiol* **59,** 71–91.

Hughes JMB & Bates DV (2003). Historical review: the carbon monoxide diffusing capacity (DLCO) and its membrane (DM) and red cell (Theta.Vc) components. *Respir Physiol Neurobiol* **138,** 115–142.

Huxley VH & Kutchai H (1981). The effect of the red cell membrane and a diffusion boundary layer on the rate of oxygen uptake by human erythrocytes. *J Physiol (Lond)* **316,** 75–83.

Ivanov II, Fedorov GE, Gus'kova RA, Ivanov KI & Rubin AB (2004). Permeability of lipid membranes to dioxygen. *Biochem Biophys Res Commun* **322,** 746–750.

Kreuzer F (1982). Oxygen supply to tissues: the Krogh model and its assumptions. *Experientia* **38,** 1415–1426.

Krogh A (1919). The number and distribution of capillaries in muscles with calculations of the oxygen pressure head necessary for supplying the tissue. *J Physiol (Lond)* **52,** 409–415.

Kutchai H (1975). Role of the red cell membrane in oxygen uptake. *Respir Physiol* **23,** 121–132.

Michenkova M, Taki S, Blosser MC, Hwang HJ, Kowatz T, Moss FJ, Occhipinti R, Qin X, Sen S, Shinn E, Wang D-K, Zeise B, Zhao P, Malmstadt N, Vahedi-Faridi A, Tajkhorshid E & Boron WF (2021). Carbon dioxide transport across membranes. *Interface Focus* **11,** 2.

Mitchell JK (1830). On the penetrativeness of fluids. *Am J Med Sci* **7,** 36–67.

Mitchell JK (1833). Art. IX. On the penetration of gases. *Am J Med Sci* **13,** 100–112.

Moll W (1968). The influence of hemoglobin diffusion on oxygen uptake and release by red cells. *Respir Physiol* **6,** 1–15.

Moss FJ, Zhao P, Salameh AI, Taki S, Wass AB, Jacobberger JW, Huffman DE, Meyerson HJ, Occhipinti R & Boron WF (2025). Role of channels in the O_2 permeability of murine red blood cells II. Morphological and proteomic studies. *bioRxiv*; DOI: https://doi.org/10.1101/2025.03.05.639962.

Nakhoul NL, Davis BA, Romero MF & Boron WF (1998). Effect of expressing the water channel aquaporin-1 on the CO_2 permeability of *Xenopus* oocytes. *Am J Physiol* **274,** C543-548.

Nicolson P & Roughton FJW (1951). A theoretical study of the influence of diffusion and chemical reaction velocity on the rate of exchange of carbon monoxide and oxygen between the red blood corpuscle and the surrounding fluid. *Proc R Soc Lond, B, Biol Sci* **138,** 241–264.

Overton E (1895). Über die osmotischen Eigenschaften der Zelle in ihrer Bedeutung für die Toxikologie und Pharmacologie. *Z Phys Chem* **22,** 189–209.

Overton E (1899). Ueber die allgemeinen osmotischen Eigenschaften der Zelle, ihre vermutlichen Ursachen und ihre Bedeutung für die Physiologie. *Vierteljahrsschr Naturforsch Ges Zürich* **44,** 88–135.

Ponder E (1948). *Hemolysis and Related Phenomena*. New York : Grune & Stratton. Available at: http://hdl.handle.net/2027/wu.89047892849.

Popel AS (1989). Theory of oxygen transport to tissue. *Crit Rev Biomed Eng* **17,** 257–321.

Richardson SL, Hulikova A, Proven M, Hipkiss R, Akanni M, Roy NBA & Swietach P (2020). Single-cell O_2 exchange imaging shows that cytoplasmic diffusion is a dominant barrier to efficient gas transport in red blood cells. *PNAS* **117,** 10067–10078.

Roughton FJ, Adair GS, Barcroft J, Goldschmidt G, Herkel W, Hill RM, Keys AB & Ray GB (1936). The thermochemistry of the oxygen-haemoglobin reaction: Comparison of the heat as measured directly on purified haemoglobin with that calculated indirectly by the Van't Hoff Isochore. *Biochem J* **30,** 2117–2133.

Roughton FJW (1932). Diffusion and chemical reaction velocity as joint factors in determining the rate of uptake of oxygen and carbon monoxide by the red blood corpuscle. *Proc R Soc Lond B* **111,** 1–36.

Roughton FJW (1964). Transport of oxygen and carbon dioxide. In *Handbook of Physiology*, pp. 767–825. American Physiological Society.

Somersalo E, Occhipinti R, Boron WF & Calvetti D (2012). A reaction-diffusion model of CO_2 influx into an oocyte. *J Theor Biol* **309,** 185–203.

Stannett V (1978). The transport of gases in synthetic polymeric membranes—an historic perspective. *J Membrane Sci* **3,** 97–115.

Strutwolf J, Zhang J, Barker AL & Unwin PR (2001). Effect of phospholipids on the kinetics of dioxygen transfer across a 1,2-dichloroethane/water interface. *Phys Chem Chem Phys* **3,** 5553–5558.

Vandegriff KD & Olson JS (1984*a*). A quantitative description in three dimensions of oxygen uptake by human red blood cells. *Biophys J* **45,** 825–835.

Vandegriff KD & Olson JS (1984*b*). The kinetics of O_2 release by human red blood cells in the presence of external sodium dithionite. *J Biol Chem* **259,** 12609–12618.

Waisbren SJ, Geibel JP, Modlin IM & Boron WF (1994). Unusual permeability properties of gastric gland cells. *Nature* **368,** 332–335.

Williams JB & Kutchai H (1986). Use of a membrane-bound fluorophore to characterize diffusion boundary layers around human erythrocytes. *Biophys J* **49,** 453–458.

Wroblewski S (1879). On the nature of the absorption of gases. *Nature* **21,** 190–192.

Yap EW & Hellums JD (1987). Use of Adair Four-Step Kinetics in Mathematical Simulation of Oxygen Transport in the Microcirculation. In *Oxygen Transport to Tissue IX*, Advances in Experimental Medicine and Biology, pp. 193–207. Springer, Boston, MA. Available at: https://link.springer.com/chapter/10.1007/978-1-4684-7433-6_22 [Accessed May 18, 2018].

Zhao P, Moss FJ, Occhipinti R, Geyer RR, Huffman DE, Gros G & Boron W F (2025). Role of channels in the O_2 permeability of murine red blood cells. I. Stopped-flow and hematological studies. *bioRxiv*; DOI: https://doi.org/10.1101/2025.03.05.639948.

Additional Information

Data availability statement

The data that support the findings of this study are available from the corresponding author upon reasonable request.

Competing interests

The authors declare that they have no competing interests.

Author contributions

R.O., P.Z. & W.F.B. designed the study; R.O. developed and implemented the computational model, and performed all numerical simulations; R.O., P.Z. and W.F. B. analyzed data. R.O. & P.Z. prepared the figures; R.O., P.Z., F.J.M., & W.F.B. wrote the manuscript.